

RADIAL TRANSPORT OF LARGE-SCALE MAGNETIC FIELDS IN ACCRETION DISKS. I. STEADY SOLUTIONS AND AN UPPER LIMIT ON THE VERTICAL FIELD STRENGTH

SATOSHI OKUZUMI¹, TAKU TAKEUCHI¹, AND TAKAYUKI MUTO²

¹Department of Earth and Planetary Sciences, Tokyo Institute of Technology, Meguro-ku, Tokyo 152-8551, Japan; okuzumi@geo.titech.ac.jp

²Division of Liberal Arts, Kogakuin University, 1-24-2, Nishi-Shinjuku, Shinjuku-ku, Tokyo 163-8677, Japan

Draft version May 12, 2019

ABSTRACT

Large-scale magnetic fields are key ingredients of magnetically driven disk accretion. We study how large-scale poloidal fields evolve in accretion disks, with the primary aim of quantifying the viability of magnetic accretion mechanisms in protoplanetary disks. We employ a kinematic mean-field model for poloidal field transport, and focus on steady states where inward advection of a field balances with outward diffusion due to effective resistivities. We analytically derive the steady-state radial distribution of poloidal fields in highly conducting accretion disks. The analytic solution reveals an upper limit on the strength of large-scale vertical fields attainable in steady states. Any excess poloidal field will be diffused away within a finite time, and we demonstrate this with time-dependent numerical calculations of the mean-field equations. We apply this upper limit to large-scale vertical fields threading protoplanetary disks. We find that the maximum attainable strength is about 0.1 G at 1 AU, and about 1 mG at 10 AU from the central star. When combined with recent magnetic accretion models, the maximum field strength translates into the maximum steady-state accretion rate of $\sim 10^{-7} M_{\odot} \text{ yr}^{-1}$, in agreement with observations. We also find the maximum field strength is ~ 1 kG at the surface of the central star provided that the disk extends down to the stellar surface. This implies that any excess stellar poloidal field of strength \gtrsim kG can be transported to the surrounding disk. This might in part resolve the magnetic flux problem in star formation.

Keywords: accretion, accretion disks – magnetic fields – magnetohydrodynamics (MHD) – planets and satellites: formation – protoplanetary disks – stars: formation

1. INTRODUCTION

Young stars host gaseous accretion disks called protoplanetary disks. They are a by-product of star formation from a molecular cloud. Observed protoplanetary disks (of age ~ 1 Myr) are characterized by an outer radius of ~ 100 AU (Kitamura et al. 2002; Andrews et al. 2009) and an accretion rate of $\sim 10^{-9}$ – $10^{-7} M_{\odot} \text{ yr}^{-1}$ (Hartmann et al. 1998; Calvet et al. 2004; Sicilia-Aguilar et al. 2005). To understand how protoplanetary disks form, evolve, and dissipate with time is essential for understanding how planets form there.

It is widely accepted that large-scale magnetic fields play key roles in disk evolution. They do not only drive turbulence via magnetorotational instability (MRI; Balbus & Hawley 1991, 1998) but also accelerate winds and outflows via the magnetocentrifugal mechanism (Blandford & Payne 1982; Spruit 1996). Both mechanisms transport angular momentum in disks, leading to accretion of disk material.

A key parameter of these accretion mechanisms is the strength of the threading poloidal field. Early local-box MHD simulations by Hawley et al. (1995) already suggested a positive dependence of the MRI-driven accretion stress on the large-scale field strength (see also Sano et al. 2004; Pessah et al. 2007). More realistic simulations including vertical gas stratification (Suzuki et al. 2010; Bai & Stone 2013a), Ohmic diffusion (Okuzumi & Hirose 2011; Gressel et al. 2012), and/or ambipolar diffusion (Simon et al. 2013a,b) have not changed this basic picture in the sense that the vertical average of the accretion stress increases with the strength of the net (large-scale) vertical field. The accretion stress produced by magnetocentrifugal winds also exhibits a positive dependence on the net poloidal field strength (Simon et al. 2013b; Bai & Stone 2013a,b; Bai

2013).

Therefore, in order to understand the evolution of accretion disks, one needs to understand the evolution of poloidal fields threading the disks. Radial transport of a large-scale poloidal field is, however, a long-standing problem in the theory of accretion disks. Early studies argued that accretion disks would advect weak interstellar magnetic field inward and build up a strong field at the center of the disks (Bisnovatyi-Kogan & Ruzmaikin 1974; Lovelace 1976). However, this picture was later confronted with a issue raised by van Ballegoijen (1989) and Lubow et al. (1994a, henceforth LPP94a). They argued that if turbulence is the source of disk accretion, then large-scale fields would be diffused away faster than they are advected inward. Their argument is as follows. Consider a turbulent disk and assume that the turbulence acts as an effective viscosity ν_{turb} on disk matter and as an effective resistivity (diffusivity) η_{turb} on large-scale magnetic fields. Then, an order-of-magnitude of the mean-field induction equation shows that significant field dragging occurs only when $\mathcal{D} \equiv (\text{Pm}_{\text{turb}} h)^{-1}$ is less than unity, where h is the disk’s aspect ratio ($\ll 1$ for thin disks) and $\text{Pm}_{\text{turb}} = \nu_{\text{turb}}/\eta_{\text{turb}}$ is the turbulent magnetic Prandtl number. The large factor h^{-1} in \mathcal{D} comes from the fact that even a slight bend of a poloidal field can lead to a high electric current density and hence to high Joule dissipation in a thin disk. One finds that if $\text{Pm}_{\text{turb}} \sim 1$ as is the case for MRI turbulence (Guan & Gammie 2009; Lesur & Longaretti 2009; Fromang & Stone 2009), the above criterion for field dragging is violated, i.e., diffusion would prevent advection of the field. This has been invoked as a challenge to the viability of magnetically driven jets and winds. This also implies that the accretion stress produced by MRI turbulence and winds would saturate at low levels. For protoplanetary disks, this

saturation level might be too low to be consistent with observations (Bai & Stone 2013b; Simon et al. 2013a).

Recently, new ideas have been raised to circumvent the fast diffusion of large-scale fields. Bisnovatyi-Kogan & Lovelace (2007) and Rothstein & Lovelace (2008) have pointed out that outward diffusion can be prevented if the disk possesses highly conductive (non-turbulent) surface layers. Recent global MHD simulations of accretion disks (Beckwith et al. 2009; Suzuki & Inutsuka 2013) show that poloidal fields do advect inward with a magnetically dominated corona or surfaces. Guilet & Ogilvie (2012, 2013) point out that fast field advection can occur even without a conductive layer because gas's advection velocity tends to increase with height (Takeuchi & Lin 2002). Spruit & Uzdensky (2005) suggest that a magnetic flux can accrete efficiently in the form of strongly magnetized patches. Taken together, these results suggest that poloidal fields can be efficiently dragged inward (i.e., \mathcal{D} can be < 1) in a realistic accretion disk.

These recent studies motivate us to ask the following questions. Assuming that advection of a poloidal field is efficient, how the radial distribution of the poloidal field will evolve with time? Can we constrain the range of the poloidal field strength for such a conducting accretion disk? What are the implications for magnetically driven evolution of accretion disks such as protoplanetary disks? Aiming at addressing these questions, we revisit global transport of large-scale magnetic fields with the assumption that poloidal fields can be efficiently dragged inward in accretion disks. As a first step of this project, we here focus on steady states where inward advection of a magnetic flux balances with outward diffusion. We employ the kinematic mean-field formalism of LPP94a and analytically derive the steady-state distribution of a poloidal field for highly conducting accretion disks. We find that there exists an upper limit on the vertical field strength for a given distance from the central star. When combined with recent models for MRI and wind-driven accretion, this upper limit suggests that magnetically driven accretion does not produce an accretion rate higher than $\sim 10^{-7} M_{\odot} \text{ yr}^{-1}$ as long as the magnetic field configuration reaches a steady state. A companion paper addresses non-steady field transport in evolving viscous accretion disks (Takeuchi & Okuzumi 2013).

The plan of the paper is as follows. In Section 2 we introduce the model to describe radial transport of magnetic fields, and derive the condition to be satisfied in steady states. In Section 3 we analytically derive the steady-state equations as well as the upper limit on the vertical field strength. Section 4 compares the analytic solution with time-dependent numerical solutions. In Section 5 we apply our result to protoplanetary systems and discuss its astrophysical implications. Section 6 is devoted to a summary.

2. MODEL

In this study, we adopt a mean-field model for large-scale poloidal fields developed by LPP94a (see Figure 1 for a schematic illustration). We take a cylindrical coordinate system (r, ϕ, z) with $r = 0$ at the disk center and $z = 0$ on the disk midplane. We denote the large-scale averages of the magnetic field strength and neutral gas velocity as \mathbf{B} and \mathbf{u} , respectively. The adopted model is kinematic in the sense that \mathbf{u} is given as a prescribed function. Any small-scale (or turbulent) motion in the disk is treated as a macroscopic magnetic diffusivity, which will also be given as a prescribed quantity (see Section 2.1 below). In principle, one can evolve \mathbf{B}

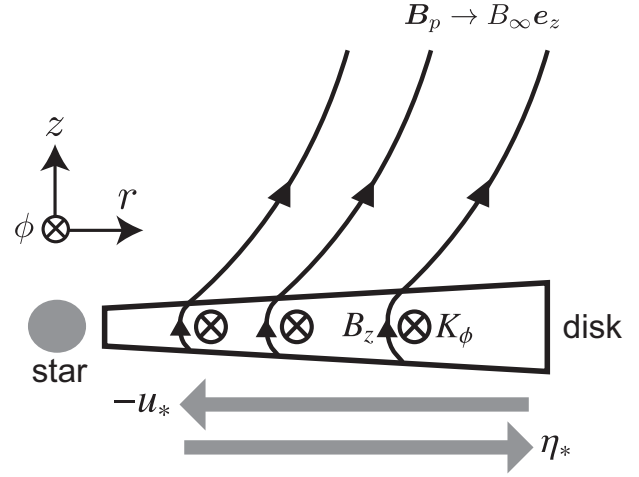


Figure 1. Schematic illustration of the mean-field model adopted in this study. The disk is assumed to be threaded by a large-scale poloidal field $\mathbf{B}_p = B_r \mathbf{e}_r + B_z \mathbf{e}_z$ (solid curves; note the field lines below the disk are omitted). The field connects to a uniform field $B_{\infty} \mathbf{e}_z$ at infinity. The flux is advected inward at some averaged speed $|u_*|$ (Equation (8)) and is diffused outward by some effective resistivity η_* (Equation (9)). The surface density of the toroidal current, K_{ϕ} , is related to the flux distribution on the disk by Biot-Savart's law (Equation (12)).

and \mathbf{u} in a self-consistent way by solving dynamical equations or adopting any empirical relation between \mathbf{B} and \mathbf{u} (see Agapitou & Papaloizou 1996), but we defer this to future work.

We assume that both \mathbf{B} and \mathbf{u} are axisymmetric, or that these quantities are already averaged in the azimuthal direction. Therefore we do not explicitly treat transport of strongly magnetized patches as considered by Spruit & Uzdensky (2005). We neglect conversion of toroidal into poloidal fields by turbulence (the so-called α dynamo), though such effects do exist in MRI-driven turbulence (e.g., Brandenburg et al. 1995; Davis et al. 2010; Gressel 2010; Simon et al. 2011; Flock et al. 2012a,b). With this assumption together with axisymmetry, no toroidal field B_{ϕ} enters the induction equation for poloidal fields. In this study, we will ignore the toroidal component of \mathbf{B} and treat the field as purely poloidal.

The accretion disk is assumed to be geometrically thin with half thickness $H \ll r$. The large-scale electric current $\mathbf{J} = (c/4\pi) \nabla \times \mathbf{B}$ is purely toroidal since \mathbf{B} is axisymmetric and poloidal. We assume that the toroidal current is well confined to the disk ($|z| < H$). The magnetic field exterior to the disk is therefore a potential field.

We express the poloidal field in terms of a flux function ψ defined as $\mathbf{B} = \nabla \times (\psi/r)$. By axisymmetry, the radial and azimuthal components of the field are written as

$$B_r = -\frac{1}{r} \frac{\partial \psi}{\partial z}, \quad (1)$$

$$B_z = \frac{1}{r} \frac{\partial \psi}{\partial r}. \quad (2)$$

The flux function is proportional to the magnetic flux $\Phi(r)$ passing through the disk interior to r , i.e.,

$$\Phi(r) = 2\pi \int_0^r B_z(r', 0) r' dr' = 2\pi \psi(r, 0). \quad (3)$$

2.1. Disk-Field Equation

The time evolution of a poloidal flux distribution is determined by the mean-field induction equation. In terms of ψ , this can be written as (see Equation 10 of LPP94a)

$$\frac{\partial \psi}{\partial t} = -u_r \frac{\partial \psi}{\partial r} - \frac{4\pi r \eta}{c} J_\phi, \quad (4)$$

where $u_r(r, z)$ is the mean radial velocity, $\eta(r, z)$ is the magnetic diffusivity (resistivity), and

$$J_\phi = \frac{c}{4\pi} (\nabla \times \mathbf{B})_\phi = \frac{c}{4\pi} \left(\frac{\partial B_r}{\partial z} - \frac{\partial B_z}{\partial r} \right) \quad (5)$$

is the toroidal component of the mean electric current. In the framework of the mean-field theory, the diffusivity in Equation (4) may be interpreted as the sum of the molecular (microscopic) diffusivity η_{mol} and the turbulent (macroscopic) diffusivity η_{turb} . Formally, Equation (4) excludes non-Ohmic diffusion which can become important in various parts of protoplanetary disks. However, if \mathbf{B} is poloidal and \mathbf{J} is toroidal as envisaged here, then ambipolar diffusion is identical to Ohmic diffusion (because $\mathbf{J} \perp \mathbf{B}$), and the toroidal component of the Hall term is zero (because the Hall term $\propto \mathbf{J} \times \mathbf{B}$).¹ In this case, it is sufficient to add the ambipolar diffusivity to η in Equation (4) (so-called Pedersen diffusivity; see, e.g., Wardle & Salmeron 2012).

For a geometrically thin disk, ψ is approximately independent of z , and therefore we are allowed to reduce Equation (4) to a one-dimensional equation with any vertical averaging (LPP94a, Ogilvie & Livio 2001). In this study, we follow Ogilvie & Livio (2001) and average the equation after weighting the “conductivity” η^{-1} . Dividing Equation (4) by η and integrating it over $-H < z < H$, we obtain the conductivity-weighted average of the induction equation (see Equation (9) of Ogilvie & Livio 2001)

$$\frac{\partial \psi}{\partial t} = -u_* \frac{\partial \psi}{\partial r} - \frac{2\pi r \eta_*}{cH} K_\phi, \quad (6)$$

where

$$K_\phi(r) \equiv \int_{-H}^H J_\phi(r, z) dz \quad (7)$$

is the toroidal component of the surface current density,

$$u_*(r) \equiv \frac{\eta_*}{2H} \int_{-H}^H \frac{u_r(r, z)}{\eta(r, z)} dz \quad (8)$$

is the conductivity-weighted average of the radial gas velocity, and

$$\frac{1}{\eta_*(r)} \equiv \frac{1}{2H} \int_{-H}^H \frac{dz}{\eta(r, z)} \quad (9)$$

is the height average of the conductivity. An advantage of the conductivity-weighted average is that the resulting induction equation (Equation (6)) does not involve the vertical distribution of J_ϕ . The vertically integrated current K_ϕ is sufficient, and this can be determined from the field configuration exterior to the disk (Ogilvie & Livio 2001, see also Section 2.2 below). Furthermore, it naturally accounts for the fact that inward advection of the flux mainly occurs at heights where the conductivity η^{-1} is high. This becomes important when an upper layer of the disk has a high conductivity

¹ Note, however, that this argument holds only when the cross-correlations of small-scale quantities arising from the non-Ohmic terms are negligible. For example, see Equation (24) of Kunz & Lesur (2013) for a mean-field equation including a cross-correlation from the Hall term.

(Bisnovatyi-Kogan & Lovelace 2007; Rothstein & Lovelace 2008) or a high accretion velocity (Guilet & Ogilvie 2012, 2013).

2.2. Exterior-Field Equation

Equation (6) requires a relation between ψ and the surface current density K_ϕ . In this study, we follow LPP94a and determine K_ϕ from Biot–Savart’s law. We assume that the current vanishes outside the disk (i.e., the exterior magnetic field is a potential field), and that the exterior field asymptotically approaches at infinity a uniform vertical field of strength B_∞ . Under these assumptions, the flux function ψ can be decomposed as (see Equation (17) of LPP94a)

$$\psi = \psi_\infty + \psi_d, \quad (10)$$

where

$$\psi_\infty(r) = \frac{1}{2} B_\infty r^2 \quad (11)$$

is the contribution from the imposed field and ψ_d is from the induced field. The latter is related to K_ϕ via Biot–Savart’s law (LPP94a)²

$$\psi_d(r) = \frac{4}{c} \int R(r_<, r_>) K_\phi(r') dr', \quad (12)$$

$$R(r_<, r_>) \equiv r_> \left[K\left(\frac{r_<}{r_>}\right) - E\left(\frac{r_<}{r_>}\right) \right], \quad (13)$$

where $r_< = \min\{r, r'\}$, $r_> = \max\{r, r'\}$, and K and E are the complete elliptic integrals defined by $K(x) = \int_0^{\pi/2} (1 - x^2 \sin^2 \theta)^{-1/2} d\theta$ and $E(x) = \int_0^{\pi/2} (1 - x^2 \sin^2 \theta)^{1/2} d\theta$. The set of Equations (6) and (12) determines the radial transport of the net poloidal flux in a disk under the assumptions we have employed.

2.3. Steady-State Condition

In this study, we focus on the steady-state solutions of Equations (6) and (12). For a steady state ($\partial \psi / \partial t = 0$), Equation (6) gives the relation between B_z and K_ϕ ,

$$B_z = \frac{2\pi D}{c} K_\phi, \quad (14)$$

where the dimensionless coefficient D is defined as

$$D \equiv -\frac{\eta_*}{u_* H} = -\frac{2}{\int_{-H}^H (u_r / \eta) dz}. \quad (15)$$

Note that we have rewritten $d\psi/dr$ in terms of B_z using Equation (2).

Equation (14) determines the bending angle of the poloidal field on the disk surface as a function of D . Substituting Equation (5) into Equation (7) and assuming that the poloidal field has dipolar symmetry, we have

$$K_\phi = \frac{c}{2\pi} B_{rs} - \frac{c}{4\pi} \frac{\partial}{\partial r} \int_{-H}^H B_z dz, \quad (16)$$

where $B_{rs} \equiv B_r|_{z=H} (= -B_r|_{z=-H})$ is the radial field strength on the disk surface. If $|B_{rs}/B_z| \gg H/r$, the second term in

² As shown in Appendix B, Equation (12) is equivalent to Equation (18) of LPP94a (see also Ogilvie 1997).

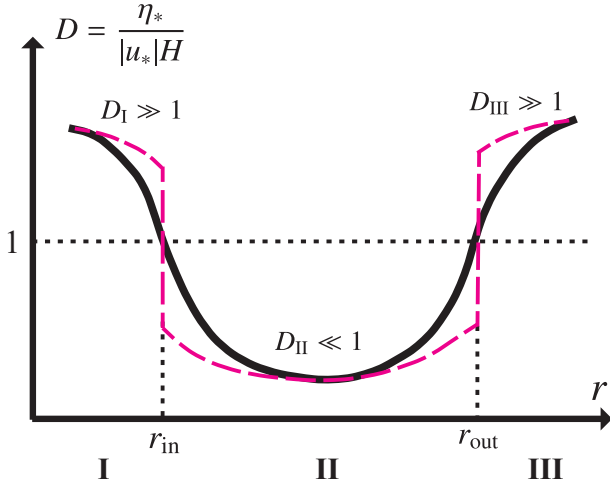


Figure 2. Schematic radial profile of D assumed in this study (solid curve). The disk is highly advecting ($D \ll 1$) in the bulk of the disk (region II), with diffusion being dominant ($D \gg 1$) only in the innermost and outermost parts of the disk (regions I and III). The three regions are defined by the boundaries where D crosses unity, $r = r_{\text{in}}$ and r_{out} . The analytic steady solution derived in Section 3 approximates the boundaries as sharp transitions as depicted by the dashed curve. Smooth transitions like the solid curve will be considered in numerical calculations (Section 4.2).

the right-hand side of Equation (16) is negligible, so Equation (14) approximately gives

$$\frac{B_{rs}}{B_z} \approx \frac{1}{D}. \quad (17)$$

This equation implies that the poloidal field lines are bent by angle i from the vertical such that $\tan i \approx 1/D$. This well explains the numerical findings of LPP94a showing that $\tan i = 1.52/(3D/2) = 1.01/D$ (see their Equation (40); note that ‘ D ’ of LPP94a differs from our D by factor 2/3).

Equation (14) does not solely determine how each of B_{rs} and B_z depends on r . In order to know this, one needs to solve Biot–Savart’s equation (Equation (12)) simultaneously with Equation (14). Section 3 will be devoted to this task.

2.4. Assumption about D and Definition of Regions

As mentioned earlier, recent theoretical studies have suggest that inward dragging of a poloidal field can efficiently take place in realistic accretion disks. We seek to understand how then a poloidal magnetic flux would be distributed in such a conductive disk. Unfortunately, the value of D is highly dependent on the vertical structure of an accretion disk, which is yet to be understood quantitatively. Therefore, in this study, we employ a simply toy model for the radial distribution of D as illustrated in Figure 2. Here, it is assumed that inward advection dominates over outward diffusion (i.e., $D < 1$) at $r_{\text{in}} < r < r_{\text{out}}$, and that the opposite happens (i.e., $D > 1$) at $r < r_{\text{in}}$ and $r > r_{\text{out}}$. We will refer to the three regions as region I, II, and III, from inside to outside (see Figure 2). In this paper, quantities in different regions will be distinguished with subscripts ‘I,’ ‘II,’ and ‘III.’ Region II corresponds the body of a highly conducting disk, while region III mimics the outermost disk region where ambipolar diffusivity is high ($\eta_* \rightarrow \infty$; see Dzyurkevich et al. 2013). The inner boundary of region II may be interpreted as the star–disk interface where accretion of matter terminates ($u_* \rightarrow 0$).

3. ANALYTIC STEADY SOLUTION

In this section, we derive the steady-state distribution of the poloidal field for the assumed distribution of D . We do this by solving Equations (14) and (12) analytically.

To make this problem analytically tractable, we for the moment assume that D sharply changes from $\gg 1$ to $\ll 1$ (and vice versa) at the boundaries $r = r_{\text{in}}$ and $r = r_{\text{out}}$ (see the dashed line in Figure 2). Thus, D is either $\gg 1$ or $\ll 1$ in the following analysis. However, as we will demonstrate in Section 4.2, the analytic solution to be derived predicts the steady-state solutions for smooth D in a surprisingly good accuracy.

In addition, we assume that the surface currents in regions I and III are so small that ψ_d is predominantly determined by the surface current in region II. Thus, we limit the interval of integration in Equation (12) to region II, $r_{\text{in}} < r' < r_{\text{out}}$. This is a good assumption since the surface current is generally suppressed in highly diffusive ($D \gg 1$) regions.

The outline of our analysis is as follows. In Section 3.1, we expand variables and equations in powers of $D_{\text{II}} (\ll 1)$. This allows us to solve Equation (14) by successive substitution. We then identify in Section 3.2 how the leading-order quantities behave away from the boundaries ($r_{\text{in}} \ll r < r_{\text{out}}$). We use the results to infer and derive the full solution for all regions, which will be done in Sections 3.3 and 3.4. Readers who are primarily interested in the final form of the solution and its implication can skip to Sections 3.4 and 3.5.

3.1. Perturbative Expansion in Powers of D_{II}

Given $D_{\text{II}} \ll 1$, we are allowed to expand all the quantities and equations in powers of D_{II} and solve the equations perturbatively. Let us expand $B_{z,\text{II}}$ and $K_{\phi,\text{II}}$ as

$$B_{z,\text{II}} = B_{z,\text{II}}^{(0)} + B_{z,\text{II}}^{(1)} + O(D_{\text{II}}^2), \quad (18)$$

$$K_{\phi,\text{II}} = K_{\phi,\text{II}}^{(0)} + O(D_{\text{II}}), \quad (19)$$

where $B_{z,\text{II}}^{(n)}, K_{\phi,\text{II}}^{(n)} = O(D_{\text{II}}^n)$ ($n = 0, 1, \dots$), and similarly for all other variables in all regions.

Substituting Equations (18) and (19) into Equation (14) and collecting terms involving the same power of D_{II} , we obtain

$$B_{z,\text{II}}^{(0)} = 0, \quad (20)$$

$$B_{z,\text{II}}^{(1)} = \frac{2\pi D_{\text{II}}(r)}{c} K_{\phi,\text{II}}^{(0)} \quad (21)$$

to first order in D_{II} . Equation (20) means that region II is completely devoid of vertical fields in the limit of $D_{\text{II}} \rightarrow 0$. The vertical field strength is nonzero only to first order in D_{II} , and is determined by the zeroth-order surface current $K_{\phi,\text{II}}^{(0)}$. It follows from Equations (2) and (20) that $\psi_{\text{II}}^{(0)}$ is independent of r and its value is determined by the flux inside region I, namely,

$$\psi_{\text{II}}^{(0)} = \psi(r_{\text{in}}) \equiv \psi_{\text{in}}, \quad (22)$$

where we have denoted the constant as ψ_{in} . From this and Equation (10), the disk-induced component of $\psi_{\text{II}}^{(0)}$ is a quadratic function of r ,

$$\psi_{d,\text{II}}^{(0)}(r) = \psi_{\text{in}} - \psi_{\infty}(r) = \psi_{\text{in}} - \frac{1}{2} B_{\infty} r^2. \quad (23)$$

This means that to zeroth order in D_{II} , the disk-induced field ($r^{-1} \partial \psi_{d,\text{II}} / \partial r$) in region II exactly cancels the imposed field

(B_z). Substituting (23) into the Biot-Savart equation (Equation (12)), we obtain the equation for $K_{\phi,II}^{(0)}$,

$$\psi_{in} - \psi_{\infty}(r) = \frac{4}{c} \int_{r_{in}}^{r_{out}} R(r_{<}, r_{>}) K_{\phi,II}^{(0)}(r') dr', \quad (24)$$

where $r_{in} < r < r_{out}$. Note that we have neglected the current in regions I and III as we already stated at the beginning of this section. The following subsections will be devoted to solve this equation.

3.2. Asymptotic Solution Deep Inside Region II

It is still not an easy task to find the solution to Equation (24). Therefore, it is useful to see how $K_{\phi,II}^{(0)}$ behaves far away from the inner and outer boundaries. To do this, let us for the moment take the limits of $r_{in} \rightarrow 0$ and $r_{out} \rightarrow \infty$. We also temporarily drop $\psi_{\infty}(r)$ in the left-hand side of Equation (24) assuming that the induced component ψ_d dominates the total flux deep inside region II (this assumption will be validated a posteriori in Section 3.3). Under these simplifications, Equation (24) reduces to

$$\psi_{in} \approx \frac{4}{c} \int_0^{\infty} R(r_{<}, r_{>}) K_{\phi,II}^{(0)}(r') dr'. \quad (25)$$

The solution to Equation (25) can be easily found by assuming $K_{\phi,II}^{(0)}$ of the power-law form

$$K_{\phi}^{(0)}(r) = Ar^{-2}, \quad (26)$$

where A is a constant. For this $K_{\phi,II}^{(0)}$, the right-hand side of Equation (25) indeed becomes a constant,

$$\begin{aligned} & \frac{4A}{c} \int_0^{\infty} R(r_{<}, r_{>}) r'^{-2} dr' \\ &= \frac{4A}{c} \int_0^1 [K(x) - E(x)] (x^{-2} + x^{-1}) dx \\ &= \frac{2\pi A}{c}, \end{aligned} \quad (27)$$

where we have used that $\int_0^1 [K(x) - E(x)] (x^{-2} + x^{-1}) dx = \pi/2$ (this can be proven with *Mathematica*). Comparing this with the left-hand side of Equation (25), we find

$$A = \frac{c\psi_{in}}{2\pi}. \quad (28)$$

Consequently, we find that $K_{\phi,II}^{(0)}$ at $r_{in} \ll r \ll r_{out}$ asymptotically behaves as

$$K_{\phi,II}^{(0)}(r) \approx \frac{c\psi_{in}}{2\pi r^2}. \quad (29)$$

Equation (29) implies that the exterior field has a split-monopole geometry (see Figure 3). We recall that $K_{\phi} \approx (c/2\pi)B_{rs}$ when $B_{rs}/B_z \gg H/r$ (see Section 2.3). Thus, Equation (29) means that $B_{rs} = \psi_{in}/r^2$ when $D_{II} \ll 1$. With this boundary condition and dipolar symmetry, potential theory tells us that the external field is a monopole field of strength $|\mathbf{B}| = \psi_{in}/(r^2 + z^2)$ except that the field above the disk has the opposite sign to the field below. The split-monopole configuration is a natural consequence of flux accumulation at the center by a highly conductive ($D \ll 1$) accretion disk (Galli & Shu 1993; Li & Shu 1997; Allen et al. 2003; Galli et al. 2006, e.g.).

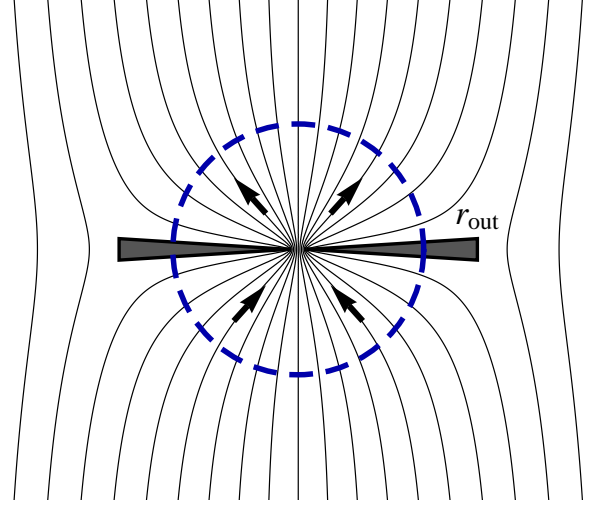


Figure 3. Split-monopole configuration of the magnetic field above and below a highly conductive ($D \ll 1$) accretion disk. The gray wedges schematically show an edge-on view of the disk, and the thin solid curves are the exterior field lines. Away from the disk, the exterior field approaches the imposed, unidirectional field B_{∞} . At $\sqrt{r^2 + z^2} \ll r_{out}$ (dashed circle) it approaches a monopolar field with the opposite polarity with respect to the equatorial plane.

From Equation (29) and the steady-state condition (Equation (21)), the asymptotic form of $B_{z,II}^{(1)}$ is

$$B_{z,II}^{(1)}(r) \approx \frac{D_{II}(r)\psi_{in}}{r^2}. \quad (30)$$

Note that $B_{z,II}^{(1)}$ does not necessarily obey a power law since D_{II} is an arbitrary function of r .

It is also possible to find the asymptotic solution in region II for arbitrary values of D_{II} as long as it is a constant. We defer the demonstration of this to Appendix A as we will not use the results in the following analysis.

3.3. Determination of ψ_{in}

The asymptotic solution derived in Section 3.2 involves ψ_{in} which is as yet undetermined. As we will show in this subsection, one can determine ψ_{in} by solving Equation (24) taking into account the presence of the imposed field, ψ_{∞} .

Let us relax the condition $r \ll r_{out}$ and instead assume $K_{\phi,II}^{(0)}$ of the form

$$K_{\phi,II}^{(0)}(r) = \frac{c\psi_{in}}{2\pi r^2} f_{out}(r). \quad (31)$$

Here, the correction factor $f_{out}(r)$ satisfies $f_{out} \rightarrow 1$ at $r \ll r_{out}$ so that Equation (31) reduces to Equation (26) there. The equation to be solved is

$$\psi_{in} - \frac{1}{2} B_{\infty} r^2 = \frac{2\psi_{in}}{\pi} \int_0^{r_{out}} R(r_{<}, r_{>}) \frac{f_{out}(r')}{r'^2} dr'. \quad (32)$$

As we will show in Appendix B.2, the requirement that the right-hand side of Equation (32) be a quadratic function of r specifies f_{out} and ψ_{in} . We defer the derivation of it to the appendix and here only show the result. We find that f_{out} is well approximated by

$$f_{out}(r) = 1 + \frac{r}{r_{out}} \left\{ \left[1 - \left(\frac{r}{r_{out}} \right)^{2\gamma} \right] - 1 \right\}, \quad (33)$$

where $\gamma = 0.45$ is the best-fit parameter. For this f_{out} , the right-hand side of Equation (32) becomes a quadratic form

$$\frac{2\psi_{\text{in}}}{\pi} \int_0^{r_{\text{out}}} R(r_{<}, r_{>}) K_{\phi, \text{II}}^{(0)}(r') dr' = \psi_{\text{in}} \left[1 - \frac{1}{2} \left(\frac{r}{r_{\text{out}}} \right)^2 \right]. \quad (34)$$

Finally, comparing this with the left-hand side of Equation (32), we find

$$\psi_{\text{in}} = B_{\infty} r_{\text{out}}^2. \quad (35)$$

It follows from Equation (35) that $\psi_{\infty}(r) \ll \psi_{\text{in}}$ at $r \ll r_{\text{out}}$, which validates the assumption we made in Section 3.2.

Comparison between Equations (11) and (35) reveals an interesting relation

$$\psi_{\text{in}} = 2\psi_{\infty}(r_{\text{out}}). \quad (36)$$

In other words, the magnetic flux threading region I is exactly twice the flux of the *imposed* field threading regions I and II. One half of ψ_{in} is simply means that the highly advecting region II flushes out all the imposed flux toward region I. Another half of ψ_{in} comes from region III: advection and diffusion near $r = r_{\text{out}}$ do transport some fraction of the imposed flux in region III to region II. An important point here is that the latter process is however limited: even a highly conducting disk cannot convey an arbitrary large poloidal flux from region III to region I. As we will see in Section 3.4, this fact sets an upper limit on the vertical field strength in region I.

For later convenience, we will also show how Equation (26) should be corrected near the inner boundary $r = r_{\text{in}}$. This correction becomes important when evaluating the magnetic flux inside region I (see Section 3.4). Let us assume $K_{\phi, \text{II}}^{(0)} = (c\psi_{\text{in}}/2\pi r^2) f_{\text{in}}(r)$, where f_{in} satisfies $f_{\text{in}} \rightarrow 1$ at $r \gg r_{\text{in}}$. Substituting this into Equation (24) and assuming $r_{\text{in}} \sim r \ll r_{\text{out}}$, we obtain the equation for f_{in} ,

$$\psi_{\text{in}} = \frac{2\psi_{\text{in}}}{\pi} \int_{r_{\text{in}}}^{\infty} R(r_{<}, r_{>}) \frac{f_{\text{in}}(r')}{r'^2} dr'. \quad (37)$$

The left-hand side of this equation requires that the right-hand side be independent of r . As shown in Appendix B.2, this requirement specifies f_{in} as

$$f_{\text{in}}(r) = \left[1 - \left(\frac{r}{r_{\text{in}}} \right)^{-2} \right]^{-1/2}. \quad (38)$$

Note that f_{in} diverges at $r = r_{\text{in}}$ but the radially integrated current $I_{\phi} = 2\pi \int r K_{\phi}(r) dr$ is still finite. The singularity merely reflects the sharp transition of the assumed D at $r = r_{\text{in}}$.

3.4. The Final Form of the Solution and an Example

To summarize the previous subsection, we have found that the surface current density in region II is given by

$$K_{\phi, \text{II}}(r) = \frac{cB_{\infty}}{2\pi} \left(\frac{r_{\text{out}}}{r} \right)^2 f_{\text{in}}(r) f_{\text{out}}(r). \quad (39)$$

This expression is correct to zeroth order in D_{II} (we will omit the superscripts “(0)” and “(1)” from this subsection onwards). The correction factors f_{in} and f_{out} are given by Equations (38) and (33), respectively. These factors are only important near the inner and outer boundaries of region II, i.e., $f_{\text{in}} \approx 1$ at $r \gg r_{\text{in}}$ and $f_{\text{out}} \approx 1$ at $r \ll r_{\text{in}}$.

We are now able to derive the radial distribution of the induced field for all regions. For region II, Equations (39) and

(21) give

$$B_{z, \text{II}} = D_{\text{II}} \left(\frac{r_{\text{out}}}{r} \right)^2 f_{\text{in}}(r) f_{\text{out}}(r) B_{\infty}, \quad (40)$$

to first order in D_{II} . For regions I and III, the Biot-Savart equation (Equation (12)) directly determines the induced flux as

$$\psi_{d, \text{I}}(r) = \frac{4}{c} \int_{r_{\text{in}}}^{r_{\text{out}}} R(r, r') K_{\phi, \text{II}} dr', \quad (41)$$

$$\psi_{d, \text{III}}(r) = \frac{4}{c} \int_{r_{\text{in}}}^{r_{\text{out}}} R(r', r) K_{\phi, \text{II}} dr', \quad (42)$$

where we have used that $(r_{<}, r_{>}) = (r, r')$ for region I and $(r_{<}, r_{>}) = (r', r)$ for region III. In Appendix C, we perform these integrations in an exact way and derive the analytic expressions for $\psi_{d, \text{I}}$ and $\psi_{d, \text{III}}$. These are given by Equations (C6) and (C14), with the corresponding field strengths by Equations (C7) and (C15), respectively.

We are particularly interested in the vertical field strength in region I. Although its exact expression is given in Appendix C (Equation (C7)), it is more instructive to derive its asymptotic expression at $r \ll r_{\text{in}}$ directly from Equation (41). For $r \ll r_{\text{in}}$, we may approximate the kernel R as $R(r, r') \approx \pi r'^2/4r'$, which follows from the asymptotic expansion of the elliptic integrals. We may also take $r_{\text{out}} \rightarrow \infty$ and hence $f_{\text{out}} \approx 1$ because the current at $r \sim r_{\text{out}}$ has little effect on the magnetic flux at $r \ll r_{\text{in}}$. Using these approximations and Equations (39) and (41), we obtain

$$\begin{aligned} \psi_{d, \text{I}}(r) &\approx \frac{1}{2} B_{\infty} r_{\text{out}}^2 r^2 \int_{r_{\text{in}}}^{\infty} \frac{f_{\text{in}}(r')}{r'^3} dr' \\ &= \frac{1}{2} \left(\frac{r_{\text{out}}}{r_{\text{in}}} \right)^2 B_{\infty} r^2. \end{aligned} \quad (43)$$

Since $\psi_{d, \text{I}} \gg \psi_{\infty}$, we may approximate the total flux ψ with $\psi_{d, \text{I}}$. Substituting this into Equation (2), we finally obtain the vertical field strength deep inside region I,

$$B_{z, \text{I}} \approx \left(\frac{r_{\text{out}}}{r_{\text{in}}} \right)^2 B_{\infty}. \quad (44)$$

Note that $B_{z, \text{I}}$ is independent of r , which is generally the case when diffusion dominates over advection.

The relation $B_{z, \text{I}} r_{\text{in}}^2 \approx B_{\infty} r_{\text{out}}^2$ is in agreement with the picture that a high conducting disk transports all the externally imposed poloidal flux to region I. It should be noted, however, that the total magnetic flux inside region I suggested by this relation is twice smaller than the actual value (see the discussion below Equation (36)). This discrepancy is explained by the fact that Equation (44) is only valid at $r \ll r_{\text{in}}$ and therefore does not account for the field near $r \sim r_{\text{in}}$. In fact, one can prove with the exact expression for $\psi_{d, \text{I}}$ (Equation (C6)) that another half of the total flux is narrowly concentrated in the vicinity of $r = r_{\text{in}}$.

We also note that the correction factor f_{in} must be properly taken into account to derive the solution for $B_{z, \text{I}}$ correctly. If one did not include the correction f_{in} in evaluating the integration in Equation (43), one would obtain $\psi_{d, \text{I}} = (1/4)(r_{\text{out}}/r_{\text{in}})^2 B_{\infty} r^2$, which is twice smaller than the correct expression in Equation (43).

So far we have neglected the current outside region II in evaluating the Biot-Savart equation. However, as $B_{z, \text{I}}$ and $B_{z, \text{III}}$ can be already known (from Equations (41) and (42)),

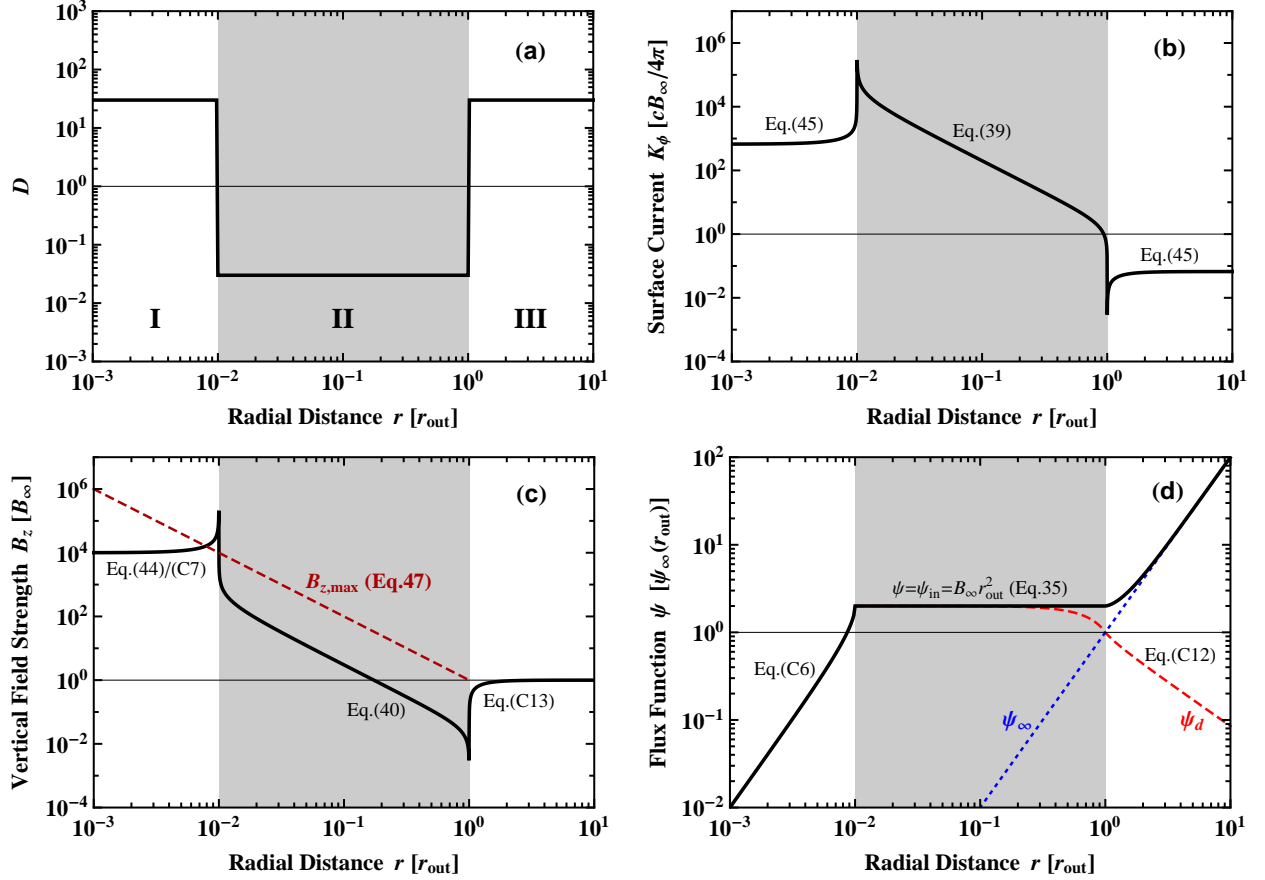


Figure 4. Steady-state solution for a piecewise constant D . The inner boundary of region II is set to $r_{\text{in}} = 0.01r_{\text{out}}$. Panel (a) displays the assumed radial profile ($D_{\text{I}} = D_{\text{III}} = 0.03$, and $D_{\text{II}} = 30$). Panels (b), (c), and (d) show the surface current density K_ϕ , vertical field strength B_z , and flux function ψ , respectively. The flux function is the sum of the contributions from the imposed fields, ψ_∞ (dotted curve), and from the induced field, ψ_d (dashed curve). Note that the spikes and valleys in the plots of B_z and K_ϕ merely reflect the discontinuities of the assumed D at the boundaries $r = r_{\text{in}}$ and r_{out} ; these features do not appear when D is smooth (see Section 4.2 and Figure 6).

$K_{\phi,\text{I}}$ and $K_{\phi,\text{III}}$ can be derived from the steady-state condition (Equation (14)), namely,

$$K_{\phi,\text{I}} = \frac{c}{2\pi D_{\text{I}}} B_{z,\text{I}}, \quad K_{\phi,\text{III}} = \frac{c}{2\pi D_{\text{III}}} B_{z,\text{III}}. \quad (45)$$

In fact, these are not necessarily small in magnitude when compared to $K_{\phi,\text{II}}$. However, this does not contradict our assumption because their contribution to the induced flux is indeed negligible as long as $D_{\text{II}} \ll 1$.

As an example, we illustrate in Figure 4 the steady solution for the case of $r_{\text{in}} = 0.01r_{\text{out}}$, $D_{\text{I}} = D_{\text{III}} = 30$, and $D_{\text{II}} = 0.03$. The same set of parameters will be considered in Section 4 where we will compare the analytic steady solution with time-dependent solutions from direct numerical integration. We will see that this steady solution is indeed materialized as a result of time evolution.

3.5. Maximum Field Strength as a Function of r

An important implication of the steady-state solution is the presence of an *upper limit* on the vertical field strength B_z attainable in steady states. To see this, let us consider how B_z at a fixed position r ($< r_{\text{out}}$) changes with changing the position of the inner boundary r_{in} . We neglect the correction factors f_{in} and f_{out} as they become important only when r is very close to r_{in} or r_{out} (furthermore, we will see in Section 4.2 that the features of these correction factors are smeared when

D is smooth). Then, from Equations (40) and (44), we find

$$B_z = \begin{cases} \left(\frac{r_{\text{out}}}{r_{\text{in}}}\right)^2 B_\infty, & r < r_{\text{in}} \text{ (region I)}, \\ D(r) \left(\frac{r_{\text{out}}}{r}\right)^2 B_\infty, & r > r_{\text{in}} \text{ (region II)}. \end{cases} \quad (46)$$

Now let us view this as a function of r_{in} and observe how B_z varies as r_{in} varies from $> r$ to $< r$. For $r_{\text{in}} > r$, B_z monotonically increases with decreasing r_{in} , and reaches a maximum $(r_{\text{out}}/r)^2 B_\infty$ at $r_{\text{in}} = r$. Once r_{in} falls below r , B_z does not exceed this value any more since $D < 1$ in region II. Thus, in the steady states, B_z at a given position is bounded from above by

$$B_{z,\text{max}}(r) = \left(\frac{r_{\text{out}}}{r}\right)^2 B_\infty. \quad (47)$$

Note that Equation (47) does not apply to region III ($r > r_{\text{out}}$) where $B_z \approx B_\infty$ (see Figure 4(c)). The dashed line in Figure 4(c) indicates Equation (47) for $r < r_{\text{out}}$.

4. COMPARISON WITH NUMERICAL SOLUTIONS

In this section, we test the steady-state solution obtained in Section 3 with numerical calculations of the original evolution equation (Equation (6)). We integrate Equations (6) and (12) using the finite-volume method described by LPP94a. We set $r_{\text{in}} = 0.01r_{\text{out}}$ and take the computational domain to

be $r_{\min} \leq r \leq r_{\max}$ with $r_{\min} = 0.03r_{\text{in}}$ and $r_{\max} = 30r_{\text{out}}$. The domain is divided into 400 logarithmically spaced cells. We use a zero-flux boundary condition for the inner boundary (i.e., $\partial\psi/\partial r = 0$ at $r = r_{\min}$) while for the outer boundary we allow the magnetic flux to flow across it by assuming that $B_z = B_\infty$ (or equivalently $\partial\psi/\partial r = rB_\infty$) at $r = r_{\max}$.

The time-dependent problem requires either η_* or u_* to be given in addition to D . Here, we prescribe η_* to be a quadratic function of r , $\eta_*(r) = r^2/t_*$, where the constant t_* has the dimension of time. is the value of η_* at $r = r_{\text{out}}$. The radial distribution of u_* is then determined according to the definition of D (Equation (15)), i.e., $u_* = -\eta_*/(DH)$. Thus, the advection speed $|u_*|$ is small in regions I and III, and is large in region II. The disk thickness H is taken so that the disk aspect ratio $h \equiv H/r$ is 0.1 for all r . All these input parameters are assumed to be independent of time t for simplicity. This restriction will be relaxed in Paper II.

The initial condition is specified by the initial distribution of the disk-induced flux ψ_d . Fiducially we will take $\psi_d(t = 0) = 0$ (i.e., $B_z = B_\infty$) throughout the computational domain, but will also consider the case where the innermost region (region I) initially possesses an induced field in excess of the steady-state value.

In the following subsections, we consider two model functions for D and present the results for each model.

4.1. Piecewise Constant D

The first model for D is a piecewise constant function given by $D_{\text{I}} = D_{\text{III}} = 30$ and $D_{\text{II}} = 0.03$. This has been already used in Section 3.4 for an illustrative purpose. The radial profile of D is shown in Figure 4(a). For the initial condition, we adopt either $B_z = B_\infty$ for all r (case A), or $B_z = 10^6 B_\infty$ for $r < r_{\text{in}}$ and $B_z = B_\infty$ for $r > r_{\text{in}}$ (case B).

Figures 5(a) and (b) display the results for the two different initial conditions (cases A and B, respectively). The dotted curves are the initial profiles of B_z , and the thin solid curves are the analytic steady solution for the assumed D (also shown in Figure 4(b)). For both cases, we find that the time-dependent numerical solution approaches to the analytic steady solution after a sufficient time. The only important difference is that region I gains the flux in case A while it loses the initial excess flux in case B. Thus, any vertical flux in excess of the steady-state value gets diffused away with time. It should be noted that details of the time evolution depend on the assumption about η_* , and are therefore not important here.

4.2. Smooth D

So far we have assumed that D sharply varies at the boundaries of region II. We here examine if our steady solution is applicable even when D smoothly connects between advective ($D < 1$) and diffusive ($D > 1$) regions. We adopt a continuous function $\log D = 1.5 \tanh[3 \log(r/r_{\text{in}})] \tanh[3 \log(r/r_{\text{out}})]$. This smoothly crosses unity at $r = r_{\text{in}}$ and $r = r_{\text{out}}$ as depicted in the top panel of Figure 6. For this model, we predict the steady-state profile of B_z in the same way as we did for piecewise constant D , i.e., by applying Equations (C7), (40), (C15) for regions I, II, and III, respectively. The predicted profile of B_z is shown in the middle panel of Figure 6 with a solid curve. Note that the profile of B_z deep inside region II ($r_{\text{in}} \ll r \ll r_{\text{out}}$) is no more given by a power law because of the radial dependence of D .

We compare this with the numerical solution of the time-dependent problem with the initial condition $B_z = B_\infty$. We

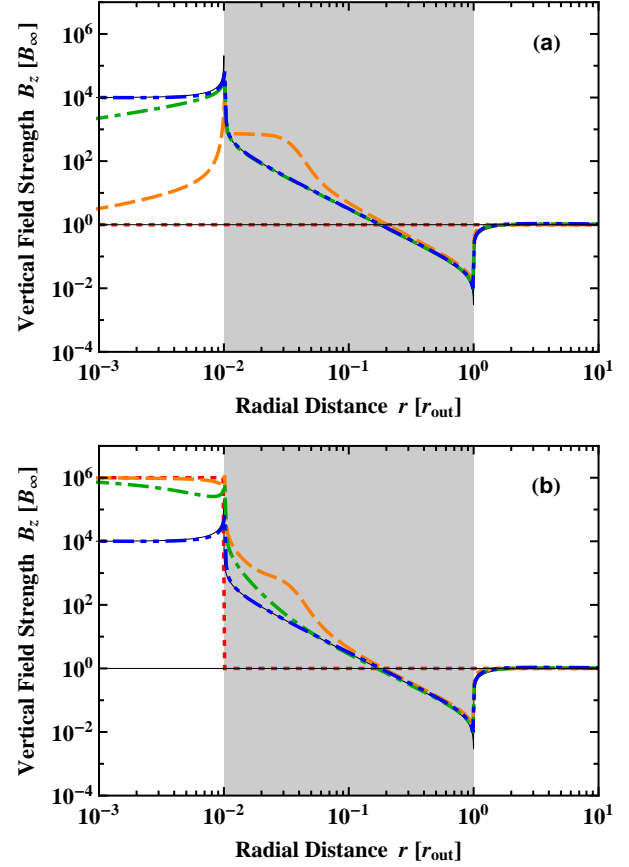


Figure 5. Comparison between analytic and time-dependent numerical solutions of Equations (6) and (12) for piecewise constant D (Section 4.1; see Figure 4(a) for the radial profile of the assumed D). Panel (a) shows the result for the initial condition $B_z = B_\infty$, while in the simulation shown in panel (b) the initial B_z is augmented by factor 10^6 at $r < r_{\text{in}}$. The dotted lines show the initial condition. The dashed, dot-dashed, and dot-dot-dashed lines are the snapshots of the numerical solutions at times $t = 0.01t_*$, $0.1t_*$, and $1.0t_*$, respectively. The solid lines are the analytic steady-state solution derived in Section 3 (also shown in Figure 4(b)). Note that the snapshots for $t = 1.0t_*$ and analytic solution are almost indistinguishable.

again see that the analytic solution well reproduces the numerical solution at late times. One exception is that the numerical solution has no visible spike or valley in B_z near $r = r_{\text{in}}$ and $r = r_{\text{out}}$ (cf. Figure 5). One might expect that the value of ψ in region II should be smaller than the prediction from the analytic solution because the peak of B_z is absent at $r = r_{\text{out}}$. However, inspection of ψ shows that its steady-state value agrees with the prediction $2\psi_\infty(r_{\text{out}})$ (Equation (35)) as long as one measures it slightly outside $r = r_{\text{out}}$. This suggests that the sharp peak in B_z is not removed but rather smeared out by the smoothed D profile. Therefore, we conclude that our analytic steady-state solution is applicable even when D is a smooth function of r , except for smeared structures near the positions where $D = 1$.

5. APPLICATION TO PROTOPLANETARY DISKS

In Section 3.5, we have derived the maximum strength on the vertical field strength in steady states. We here apply this result to protoplanetary disk systems and discuss its astrophysical implications. As a reference value, we take $r_{\text{out}} = 100$ AU from millimeter observations of T-Tauri disks (e.g., Kitamura et al. 2002; Andrews et al. 2009), and $B_\infty = 10 \mu\text{G}$ from Zeeman observations of molecular clouds (e.g.,

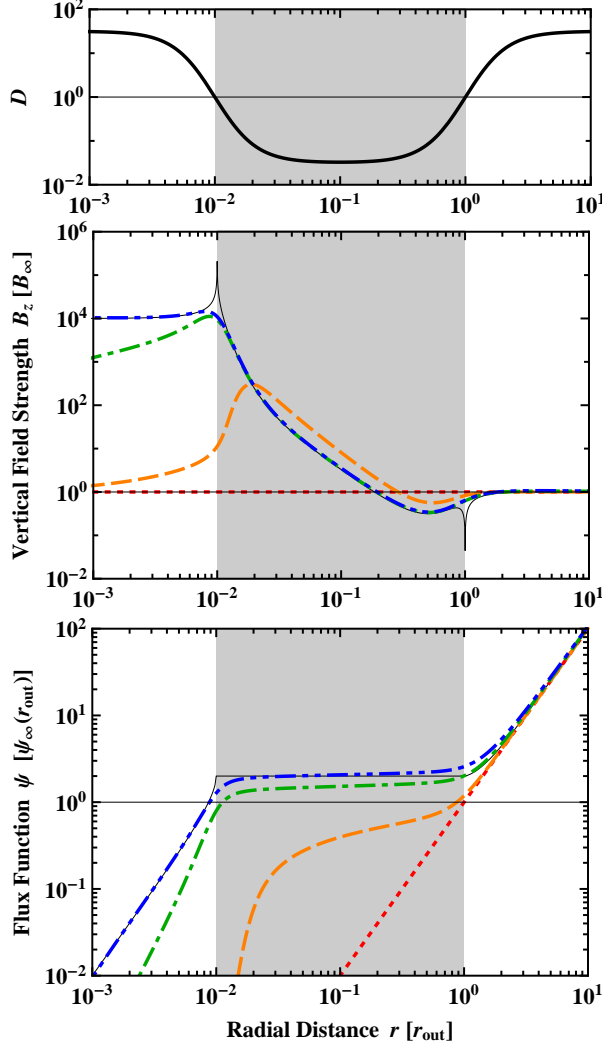


Figure 6. Comparison between analytic and time-dependent numerical solutions of Equations (6) and (12) for smooth D (Section 4.2). The upper panel shows the assumed D , and the lower panel show the result. The initial condition is $B_z = B_\infty$ for all r (dotted line). The dashed, dot-dashed, and dotted lines are the snapshots of the numerical calculations at $t = 0.01t_*$, $0.1t_*$, and $1.0t_*$, respectively.

Troland & Crutcher 2008; Crutcher et al. 2009). Then, Equation (47) predicts

$$B_{z,\max}(r) = 0.1 r_{\text{AU}}^{-2} \left(\frac{r_{\text{out}}}{100 \text{ AU}} \right)^2 \left(\frac{B_\infty}{10 \mu\text{G}} \right) \text{G}, \quad (48)$$

where $r_{\text{AU}} = r/1 \text{ AU}$. The solid line in Figure 7 shows the radial distribution of $B_{z,\max}$ for the case of $B_\infty = 10 \mu\text{G}$ and $r_{\text{out}} = 100 \text{ AU}$.

5.1. Upper Limits on the Accretion Rate

The primary purpose of this study is to understand the evolution of protoplanetary disks in the framework of magnetic accretion scenarios. As mentioned earlier, both MRI-driven and wind-driven accretion mechanisms predict that the mass accretion rate \dot{M} depends on the strength of the net (large-scale) vertical field. In this subsection, we synthesize Equation (48) and existing theoretical predictions for the \dot{M} – B_z relation to constrain the range of the accretion rate attainable by these accretion mechanisms.

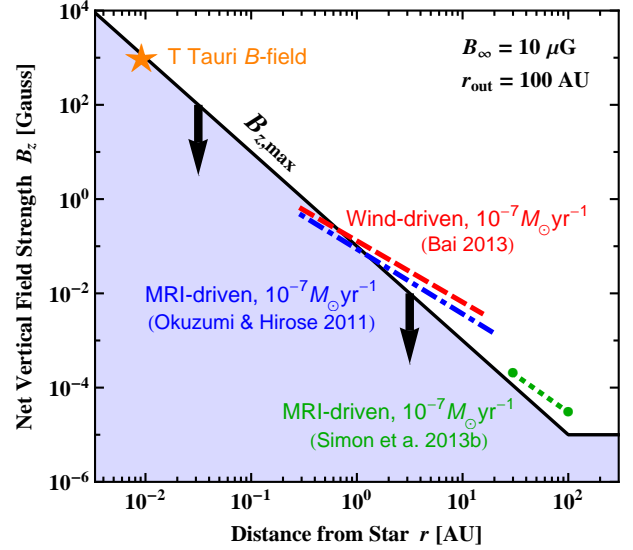


Figure 7. The upper limit on the large-scale vertical field strength, $B_{z,\max}$ (Equation (48); solid line), for $B_\infty = 10 \mu\text{G}$ and $r_{\text{out}} = 100 \text{ AU}$. The dot-dashed, dashed, and dotted lines show theoretical predictions for the vertical field strength required for disk accretion of $\dot{M} = 10^{-7} M_\odot \text{yr}^{-1}$ (see Section 5.1 for details). The star symbol marks the typical field strength and radius of observed T Tauri stars.

Because protoplanetary disks are poorly ionized, MRI and winds in the disks are highly susceptible to non-ideal MHD effects. Lacking an establish accretion model accounting for all the non-ideal effects, we employ two existing models in parallel. We first consider the classical scenario where only Ohmic diffusion is taken into account. For this case, Okuzumi & Hirose (2011) empirically obtained the \dot{M} – B_z relation for MRI-driven turbulence. They found that if Ohmic diffusion suppresses MRI near the midplane then the relation is given by³

$$\alpha \approx 530 \beta_{z0}^{-1}. \quad (49)$$

Here, α is the the height-averaged turbulent stress normalized by the height-averaged pressure (also known as the Shakura–Syunyaev α parameter), and β_{z0} is the plasma beta for the net vertical flux measured at the midplane. In steady states, α is related to \dot{M} as $\dot{M} = 2\pi\alpha\Sigma c_s^2/\Omega$, where Ω is the orbital frequency, Σ is the gas surface density, and c_s is the sound speed (see, e.g., Section III.A of Balbus & Hawley 1998; Equation (19) of Simon et al. 2013a). The midplane plasma beta is related to the net vertical field strength B_z as $\beta_{z0} = 8\pi\Sigma c_s^2/\sqrt{2\pi}B_z^2 H_g$, where $H_g = c_s/\Omega$ is the pressure scale height of the disk. If we use these relations, Equation (49) translates into the \dot{M} – B_z in physical units,

$$\dot{M} \approx 330 \frac{H_g}{\Omega} B_z^2. \quad (50)$$

Note that \dot{M} is independent of the disk mass since $\alpha \propto \dot{M}/\Sigma$ while $\beta_{z0} \propto \Sigma/B_z^2$. This reflects the fact that the Maxwell stress does not explicitly involve the gas density (see Wardle 2007 and Bai 2011 for a similar expression).

Let us see how $B_{z,\max}$ constrains the accretion rate given by Equation (50). Here, we assume a protoplanetary disk around

³ Equation (49) follows from Equations (18), (28), and (29) of Okuzumi & Hirose (2011) with the assumption that the vertical width of the dead zone ($H_{\text{res},0}$ and $H_{\Lambda,0}$ of OH11) is comparable to the pressure scale height H_g .

a solar-type star, and adopt $\Omega = 2.0 \times 10^{-7} r_{\text{AU}}^{-3/2} \text{ s}^{-1}$ and $H_g = 0.033 r_{\text{AU}}^{5/4} \text{ AU}$ following Hayashi (1981). Substituting these into Equation (50), we obtain

$$\dot{M} \approx 1.3 \times 10^{-7} r_{\text{AU}}^{11/4} \left(\frac{B_z}{0.1 \text{ G}} \right)^2 M_{\odot} \text{ yr}^{-1}. \quad (51)$$

This gives the MRI-driven accretion rate for given B_z . Applying the constraint $B < B_{z,\text{max}}$ to the above relation, we obtain $\dot{M} \lesssim 1 \times 10^{-7} M_{\odot} \text{ yr}^{-1}$ at $r = 1 \text{ AU}$ and $\dot{M} \lesssim 0.7 \times 10^{-8} M_{\odot} \text{ yr}^{-1}$ at $r = 10 \text{ AU}$. For reference, the dashed line in Figure 7 shows the value of B_z required for $\dot{M} = 10^{-7} M_{\odot} \text{ yr}^{-1}$ predicted by Equation (51).

A similar constraint is derived from the more recent scenario including ambipolar diffusion. Recent MHD simulations by Bai & Stone (2013b) and Bai (2013) have suggested that accretion at $0.3 \text{ AU} \lesssim r \lesssim 15 \text{ AU}$ is mainly driven by magnetocentrifugal winds because ambipolar diffusion completely suppressed MRI there. The relation between the wind-driven \dot{M} and B_z has been provided by Bai (2013), which reads

$$\dot{M} = 0.91 \times 10^{-8} r_{\text{AU}}^{1.21} \left(\frac{B_z}{10 \text{ mG}} \right)^{0.93} M_{\odot} \text{ yr}^{-1}. \quad (52)$$

Note that \dot{M} is again independent of Σ (see Bai (2013) for more discussions). If we apply $B < B_{z,\text{max}}$ to Equation (52), we obtain $\dot{M} \lesssim 0.8 \times 10^{-7} M_{\odot} \text{ yr}^{-1}$ at $r = 1 \text{ AU}$ and $\dot{M} \lesssim 2 \times 10^{-8} M_{\odot} \text{ yr}^{-1}$ at $r = 10 \text{ AU}$. The dashed line shows the value of B_z required for $\dot{M} = 10^{-7} M_{\odot} \text{ yr}^{-1}$ predicted by Equation (52).

Further out in the disks, MRI operates even in the presence of ambipolar diffusion. MHD simulations by Simon et al. (2013a,b) show that \dot{M} increases with B_z and reaches $10^{-7} M_{\odot} \text{ yr}^{-1}$ at $B_z \sim 200 \mu\text{G}$ for $r = 30 \text{ AU}$, and at $30 \mu\text{G}$ for $r = 100 \text{ AU}$. These values are marked in Figure 7 by the filled circles connected by the dotted line. We find that the required field strengths are close to the upper limit $B_{z,\text{max}}$, which suggests that $\dot{M} \lesssim 10^{-7} M_{\odot} \text{ yr}^{-1}$ for these regions.

Taken together, all these models suggest that the upper limit on the magnetically driven accretion rate is $\sim 10^{-7} M_{\odot} \text{ yr}^{-1}$. This is consistent with upper limits suggested by observations (Hartmann et al. 1998; Calvet et al. 2004; Sicilia-Aguilar et al. 2005).

5.2. Possible Relevance to the “Magnetic Flux Problem” in Star Formation

Another interesting application of Equation (48) is to the so-called magnetic flux problem in star formation (Nakano 1984). Young stars are known to have a magnetic field of typical strength $\sim \text{kG}$ (e.g., Johns-Krull 2007). Star-forming dense cores of molecular clouds also have a magnetic field (Troland & Crutcher 2008; Crutcher et al. 2009), but the magnetic flux of a single core is about four orders of magnitude larger than that of a single young star. Therefore, the magnetic flux that was inherited from the parent cloud must have dissipated, at least to a $\lesssim \text{kG}$ level, by the time the star became visible. Ohmic dissipation during star formation is one plausible solution to this problem (e.g., Nakano et al. 2002; Shu et al. 2006; Machida et al. 2007; Dapp et al. 2012). Other possibilities include flux destruction after the external field detaches from the star (Braithwaite 2012).

Here, we explore the possibility that the excess flux is lost through transport between the star and surrounding protoplan-

etary disk. Let us suppose that a protoplanetary disk extends to a central star and hence Equation (48) is applicable down to the interface between the disk and star. Then, Equation (48) suggests that $B_{z,\text{max}} \approx 1 \text{ kG}$ at protostellar radius $\approx 2R_{\odot} \approx 10^{-2} \text{ AU}$ for the selected parameters $B_{\infty} = 10 \mu\text{G}$ and $r_{\text{out}} = 100 \text{ AU}$ (see the star symbol in Figure 7). Interestingly, the predicted $B_{z,\text{max}}$ is in good agreement with the observed stellar field strengths. Any excess flux above this level will be lost after a sufficient time (as demonstrated in Figure 5(b)) if the flux transport is allowed across the star-disk interface (for example, convection inside the star might effectively diffuse the flux toward the stellar surface). If this mechanism is viable, then this might partly resolve the long-standing problem of star formation theory. Further examination of this possibility is, however, beyond the scope of this paper.

6. SUMMARY AND DISCUSSION

In this study, we have studied how a large-scale poloidal field is transported in a highly conducting accretion disk, primarily aiming at understanding the viability of magnetically driven accretion mechanisms. We have employed the kinematic mean-field model for a large-scale poloidal field originally developed by LPP94a. As a first step, we have focused on steady states where inward advection of a poloidal field balances with outward diffusion. In a companion paper (Takeuchi & Okuzumi 2013), we extend our analysis to time-dependent problems and study how poloidal fields are transported in evolving accretion disks.

We have analytically derived the steady-state distribution of a poloidal field for conducting accretion disks. The most important conclusion drawn from this analytic solution is that there is an upper limit on the large-scale vertical field strength attainable in steady states (Equation (47)). The upper limit is given by a function of the distance from the central star (r), the poloidal strength at infinity (B_{∞}), and the outer radius of the highly conductive region (r_{out}). For $r_{\text{out}} = 100 \text{ AU}$ and $B_{\infty} = 10 \mu\text{G}$, the maximum vertical field strength is about 0.1 G at $r = 1 \text{ AU}$, and about 1 mG at $r = 10 \text{ AU}$ (Equation (48); Figure 7). Any poloidal field of a strength above the limit will be eventually diffused away outward on the diffusion timescale. We have demonstrated this with a time-dependent numerical calculations of the mean-field equations.

We have applied this upper limit to a large-scale poloidal field threading a protoplanetary disk around a young star. We have adopted three different theoretical models for magnetically driven accretion (Okuzumi & Hirose 2011; Bai 2013; Simon et al. 2013b) to translate the large-scale vertical field strength into the accretion rate. We have found that all these models suggest a maximum steady-state accretion rate of $\sim 10^{-7} M_{\odot} \text{ yr}^{-1}$. This is in agreement with observations showing that $\dot{M} \sim 10^{-9} - 10^{-7} M_{\odot} \text{ yr}^{-1}$ for T Tauri stars.

We have also applied the upper limit to the flux of young stars assuming that surrounding protoplanetary disks extend to the stellar surfaces. We find that the maximum field strength is $\sim 1 \text{ kG}$ at the surface of the central star. This implies that any excess stellar poloidal field of strength $\gtrsim \text{kG}$ can be lost via outward diffusion to the circumstellar disks. That mechanism might explain why observed young stars have a significantly small magnetic flux compared to molecular cloud cores.

The analysis presented in this study has employed a number of simplifications, and there are at least three important caveats that should be mentioned. First, we have assumed

that all important parameters are independent of time, which is of course not valid when the gas disk evolves faster than the poloidal field. For this case, the poloidal-field distribution largely depends on the initial condition as we will discuss in a companion paper (Takeuchi & Okuzumi 2013). Second, the treatment of the exterior field as a potential field is formally incompatible with magnetically driven outflows. Therefore, our results might not apply when outflows create strong currents above the disk. Finally, it has been suggested that wind-driven accretion can become unstable (Lubow et al. 1994b; Cao & Spruit 2002; Moll 2012), for which case our steady-state solution would be inapplicable.

The authors thank Takeru Suzuki, Hidekazu Tanaka, and Shu-ichiro Inutsuka for useful discussion. This work was supported by Grant-in-Aid for Research Activity Start-up (#25887023) from JSPS, and by Grants-in-Aid for Scientific Research (#20540232, 23103005) from MEXT.

APPENDIX

A. ASYMPTOTIC SOLUTION IN REGION II FOR ARBITRARY CONSTANT D_{II}

In this appendix, we consider cases where D_{II} is constant but not necessarily small. For these cases, Equations (12) and (14) become self-similar with respect to r in the limit of $r_{\text{in}} \ll r \ll r_{\text{out}}$ and $\psi_{\infty} \ll \psi_d$, and therefore the solution must be written as a power law. Specifically, if we suppose $K_{\phi} \propto r^{-q}$ with q being a constant, then a dimensional analysis shows $B_z \propto r^{-q}$ and $\psi \propto r^{2-q}$. As we will see below, the exponent q is determined as a function of D_{II} .

Below we omit the subscript “II” for the sake of clarity. In the limit of $r_{\text{in}} \ll r \ll r_{\text{out}}$ and $\psi_{\infty} \ll \psi_d$, Equation (12) reduces to

$$\psi = \frac{4}{c} \int_0^{\infty} R(r_<, r_>) K_{\phi}(r') dr'. \quad (\text{A1})$$

Note that the perturbative approach employed in Section 3.1 is not used here as it only applies to $D \ll 1$. Let us assume

$$K_{\phi}(r) = Ar^{-q}, \quad (\text{A2})$$

where A and q are constants. Substituting Equation (A2) into Equation (A1), we obtain

$$\psi = \frac{2\pi C(q)}{c} Ar^{2-q}, \quad (\text{A3})$$

where

$$C(q) \equiv \frac{2}{\pi} \int_0^1 [K(x) - E(x)] (x^{-q} + x^{q-3}) dx \quad (\text{A4})$$

is a numerical coefficient that depends on q . For $0 < q < 3$, the integration in the right-hand side of Equation (A4) converges, resulting in

$$C(q) = \frac{2}{3\pi} \left[{}_3F_2 \left(1, 1, \frac{4-q}{2}; \frac{3}{2}, \frac{5}{2}; 1 \right) + {}_3F_2 \left(1, 1, \frac{q+1}{2}; \frac{3}{2}, \frac{5}{2}; 1 \right) \right], \quad (\text{A5})$$

where ${}_3F_2$ is a generalized hypergeometric function. It is useful to note that $C(1) = C(2) = 1$.

The induced vertical field is

$$\begin{aligned} B_z &= \frac{1}{r} \frac{d\psi}{dr} = \frac{2\pi(2-q)C(q)}{c} Ar^{-q} \\ &= \frac{2\pi(2-q)C(q)}{c} K_{\phi}. \end{aligned} \quad (\text{A6})$$

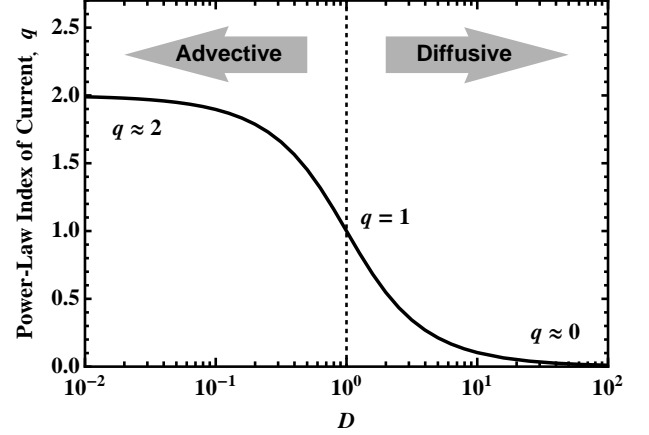


Figure 8. Power-law index q for radially constant D .

Comparing this with Equation (14), we obtain the equation for q ,

$$(2 - q)C(q) = D. \quad (\text{A7})$$

Figure 8 plots the solution of Equation (A7) as a function of D . We see that q monotonically increases with decreasing D , meaning that the radial profiles of B_z and K_{ϕ} become steeper as inward advection becomes more effective. The asymptotic values are $q \rightarrow 2$ for $D \rightarrow 0$ and $q \rightarrow 0$ for $D \rightarrow \infty$. The solution for $D \rightarrow \infty$ just shows that the vertical field strength becomes uniform in r in the limit where diffusion dominates over advection.

B. INVERTING BIOT-SAVART'S INTEGRAL EQUATION

In this appendix, we present an analytic method to invert Biot–Savart’s equation. In an integral form, the Biot–Savart’s law can be written as (see, e.g., Jackson 1998)

$$\frac{\psi_d(r)}{r} = \frac{1}{c} \int_{r_{\text{in}}}^{r_{\text{out}}} r' dr' \int_0^{2\pi} d\phi' \frac{K_{\phi}(r') \cos \phi'}{(r^2 + r'^2 - 2rr' \cos \phi')^{1/2}} \quad (\text{B1})$$

(as shown below, this is equivalent to Equation (12) in the main text). We seek for K_{ϕ} that gives a flux function of the form $\psi_d \propto \text{constant} - r^2$ or $\psi_d \propto \text{constant}$.

To begin with, we perform azimuthal integration in these equations. The integration can be written in terms of the Laplace coefficient known in celestial mechanics (see, e.g., Murray & Dermott 1999). The series expansion of the Laplace coefficient gives

$$\int_0^{2\pi} \frac{\cos \phi' d\phi'}{(r^2 + r'^2 - 2rr' \cos \phi')^{1/2}} = \frac{\pi}{r_>} \sum_{n=0}^{\infty} c_n \left(\frac{r_<}{r_>} \right)^{2n+1}, \quad (\text{B2})$$

$$c_n = \frac{(\frac{1}{2})_n (\frac{3}{2})_n}{(1)_n (2)_n}, \quad (\text{B3})$$

where $(a)_n = a(a+1) \cdots (a+n-1)$ is the Pochhammer symbol. One can show, by using Equation (B2) together with the relations $\sum_{n=0}^{\infty} c_n \alpha^{2n+1} = (4/\pi\alpha)[K(\alpha) - E(\alpha)]$ and $rr'/r_< = r_>$, that Equation (B1) is equivalent to Equation (12). Putting Equation (B2) into Equation (B1), we obtain Biot–Savart’s

equation after azimuthal integration,

$$\psi_d = \frac{\pi}{c} \sum_{n=0}^{\infty} c_n \left[\frac{1}{r^{2n+1}} \int_{r_{\text{in}}}^r r'^{2n+2} K_\phi dr' + r^{2(n+1)} \int_r^{r_{\text{out}}} \frac{K_\phi dr'}{r'^{2n+1}} \right], \quad (\text{B4})$$

for $r_{\text{in}} < r < r_{\text{out}}$.

B.1. Analogy with Inverse Problems for Gravitational Fields

Before we proceed, it is useful to see how our problem resembles inverse problems of axisymmetric *scalar* fields. As pointed out by LPP94a, solving Biot–Savart’s equation for K_ϕ is analogous to finding the surface density distribution of a disk for given gravitational potential distribution. For example, for an axisymmetric disk with surface density profile $\Sigma(r)$, the gravitational potential $\Phi(r)$ is given by

$$\Phi(r) = -G \int_{r_{\text{in}}}^{r_{\text{out}}} r' dr' \int_0^{2\pi} d\phi' \frac{\Sigma(r')}{(r^2 + r'^2 - 2rr' \cos \phi')^{1/2}}, \quad (\text{B5})$$

where G is the gravitational constant. Equation (B5) is identical to Equation (B1) if we replace $G\Sigma(r') \rightarrow K_\phi(r') \cos \phi'$ and $\Phi \rightarrow -c\psi_d/r$. A similar equation can be found in the problem of finding the pressure distribution $P(r)$ on the interface of two elastic spheres for given surface displacement distribution $u_z(r)$, in which case $G\Sigma \rightarrow P$ and $\Phi \rightarrow -\pi E^* u_z$, where E^* is the reduced Young modulus (Johnson 1987; Landau & Lifshitz 1986).

It is known that Equation (B5) has two types of exact solutions in the limit of $r_{\text{in}} \rightarrow 0$. The first type is

$$\Sigma(r) = \left[1 - \left(\frac{r}{r_{\text{out}}} \right)^2 \right]^{1/2} \Sigma_c, \quad (\text{B6})$$

where Σ_c is a constant. Equation (B6) gives a harmonic gravitational potential

$$\Phi(r) = -\frac{\pi^2 G \Sigma_c r_{\text{out}}}{2} \left[1 - \frac{1}{2} \left(\frac{r}{r_{\text{out}}} \right)^2 \right]. \quad (\text{B7})$$

The second type is

$$\Sigma(r) = \left[1 - \left(\frac{r}{r_{\text{out}}} \right)^2 \right]^{-1/2} \Sigma_c, \quad (\text{B8})$$

where Σ_c is a constant. Equation (B8) gives a constant potential

$$\Phi = -\pi^2 G \Sigma_c r_{\text{out}}. \quad (\text{B9})$$

In contact mechanics ($\Sigma \rightarrow P$ and $\Phi/G \rightarrow -\pi E^* u_z$), the first and second types are known as Hertz’s and Boussinesq’s solutions, respectively (Johnson 1987; Landau & Lifshitz 1986). These solutions are useful when we guess the functional form of K_ϕ for given ψ_d .

B.2. Solution near the Outer Boundary

We first solve Equation (B4) for $\psi_d = \psi_{\text{in}} - B_\infty r^2/2$ (Equation (23)). In this subsection, we focus on how the solution behaves near the outer boundary ($r \sim r_{\text{out}}$), and for this reason we will take r_{in} to be zero. As described in the main text, the asymptotic behavior of the solution $r \ll r_{\text{out}}$ shows that the solution must be of the form $K_\phi(r') = (c\psi_{\text{in}}/2\pi r'^2) f_{\text{out}}(r')$ (Equation (29)), where f_{out} satisfies $f_{\text{out}} \rightarrow 1$ as $r'/r_{\text{out}} \rightarrow 0$.

To carry out the integration in Equation (B4), we expand f_{out} in powers of r'/r_{out} ,

$$f_{\text{out}}(r') = 1 + \sum_{m=0}^{\infty} a_{2m+1} \left(\frac{r'}{r_{\text{out}}} \right)^{2m+1}, \quad (\text{B10})$$

where a_{2m+1} ($m = 0, 1, 2, \dots$) are constants, and we have used that $f_{\text{out}} \rightarrow 1$ as $r'/r_{\text{out}} \rightarrow 0$. We have assumed that K_ϕ does not involve terms r'^{2m} ($m = 1, 2, \dots$) because such terms would yield unwanted logarithmic terms in the resultant $\psi_d(r)$.

With Equation (B10), the integration in Equation (B4) can be analytically performed. The result reads,

$$\begin{aligned} \psi_d = & \frac{\psi_{\text{in}}}{2} \sum_{n=0}^{\infty} c_n \left[\frac{1}{2(n+1)} + \frac{1}{2n+1} \right] \\ & + \frac{\psi_{\text{in}}}{2} \sum_{m=0}^{\infty} a_{2m+1} \left(\frac{r}{r_{\text{out}}} \right)^{2m+1} \\ & \times \sum_{n=0}^{\infty} c_n \left[\frac{1}{2(n+m+1)} + \frac{1}{2(n-m)+1} \right] \\ & + \frac{\psi_{\text{in}}}{2} \sum_{n=0}^{\infty} c_n \left(\frac{r}{r_{\text{out}}} \right)^{2(n+1)} \left[-\frac{1}{2(n+1)} + \sum_{m=0}^{\infty} \frac{a_{2m+1}}{2(m-n)-1} \right]. \end{aligned} \quad (\text{B11})$$

This result can be simplified if we use the relation

$$\begin{aligned} & \sum_{n=0}^{\infty} c_n \left[\frac{1}{2(n+m+1)} + \frac{1}{2(n-m)+1} \right] \\ & = \frac{{}_3F_2\left(\frac{1}{2}, \frac{3}{2}, m+1; 2, m+2; 1\right)}{2(m+1)} + \frac{{}_3F_2\left(\frac{1}{2}, \frac{3}{2}, \frac{1-2m}{2}; 2, \frac{3-2m}{2}; 1\right)}{1-2m} \\ & = \begin{cases} 2, & m=0, \\ 0, & m=1, 2, \dots \end{cases} \end{aligned} \quad (\text{B12})$$

(one can verify this with *Mathematica*). With this relation, we obtain

$$\begin{aligned} \psi_d = & \psi_{\text{in}} + \frac{\psi_{\text{in}} a_1 r}{r_{\text{out}}} \\ & + \frac{\psi_{\text{in}}}{2} \sum_{n=0}^{\infty} c_n \left(\frac{r}{r_{\text{out}}} \right)^{2(n+1)} \left[-\frac{1}{2(n+1)} + \sum_{m=0}^{\infty} \frac{a_{2m+1}}{2(m-n)-1} \right]. \end{aligned} \quad (\text{B13})$$

Comparing this with $\psi_d = \psi_{\text{in}} - B_\infty r^2/2$, we find that the second term of Equation (B13) must vanish, and that the infinite sum in the third term must leave a term proportional to r^2 . Hence, the coefficients a_1, a_3, a_5, \dots must satisfy the relations

$$a_1 = 0, \quad (\text{B14})$$

$$\sum_{m=1}^{\infty} \frac{a_{2m+1}}{2(m-n)-1} = \frac{1}{2(n+1)} \quad n = 1, 2, \dots \quad (\text{B15})$$

Unfortunately, we could not find the set of a_{2m+1} that exactly satisfies Equation (B15). However, an approximate, but fully accurate solution can be obtained if we note that the flux function under consideration is of the same functional form as the harmonic gravitational potential (Equation (B7)). By analogy with Equation (B6), let us consider the following ansatz

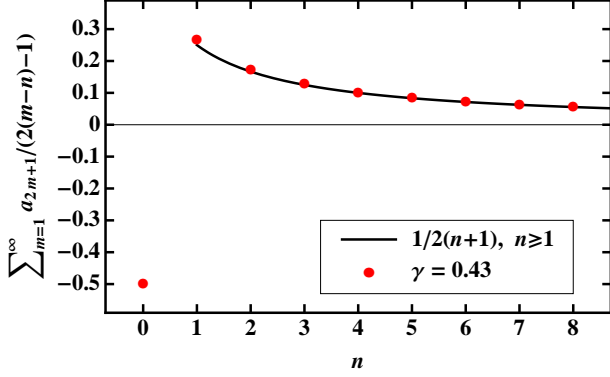


Figure 9. Values of $\sum_{m=1}^{\infty} \frac{a_{2m+1}}{2(m-n)-1}$ ($n = 0, 1, 2, \dots$) for $\gamma = 0.43$ (circles) from Equation (B18). The curve indicates the right-hand side of Equation (B15), $\frac{1}{2(n+1)}$ ($n \geq 1$).

for f_{out} ,

$$f_{\text{out}}(r') = 1 + \frac{r'}{r_{\text{out}}} \left\{ \left[1 - \left(\frac{r'}{r_{\text{out}}} \right)^2 \right]^{\gamma} - 1 \right\}, \quad (\text{B16})$$

where γ is a fitting parameter to be determined below. We may assume $\gamma > -1$ since otherwise the radially integrated current $2\pi \int_0^{r_{\text{out}}} K_{\phi}(r') r' dr'$ would diverge. The ansatz is equivalent to Equation (B10) with $a_1 = 0$ and

$$a_{2m+1} = \frac{(-1)^m}{m!} \frac{\Gamma(\gamma+1)}{\Gamma(\gamma+1-m)}, \quad m = 1, 2, \dots \quad (\text{B17})$$

This ansatz is useful because the infinite sum $\sum_{m=1}^{\infty} \frac{a_{2m+1}}{2(m-n)-1}$ has a closed expression

$$\sum_{m=1}^{\infty} \frac{a_{2m+1}}{2(m-n)-1} = \frac{1}{1+2n} + \frac{\Gamma(-\frac{1}{2}-n)\Gamma(1+\gamma)}{2\Gamma(\frac{1}{2}-n+\gamma)}. \quad (\text{B18})$$

By a least-square method, we find that the right-hand side of Equation (B18) best approximates that of Equation (B15) when $\gamma = 0.43$ (Figure 9).

In the main text we have introduced ψ_{in} as an undetermined quantity. As we will see below, this quantity is determined as an *eigenvalue* of the inversion problem under consideration. Substitution of Equations (B14) and (B15) into Equation (B13) shows that ψ_d must be of the form

$$\psi_d = \psi_{\text{in}} + \frac{\psi_{\text{in}}}{2} \left(-\frac{1}{2} + \sum_{m=0}^{\infty} \frac{a_{2m+1}}{2m-1} \right) \left(\frac{r}{r_{\text{out}}} \right)^2, \quad (\text{B19})$$

where we have used that $c_0 = 1$. The infinite sum remaining in the above equation can be evaluated as $\sum_{m=1}^{\infty} \frac{a_{2m+1}}{2m-1} \approx -0.502 \approx -1/2$ if we use Equation (B18) with the best-fit $\gamma = 0.43$ (see also Figure 9). Thus, we find

$$\psi_d = \psi_{\text{in}} \left[1 - \frac{1}{2} \left(\frac{r}{r_{\text{out}}} \right)^2 \right]. \quad (\text{B20})$$

Imposing that this is equal to $\psi_{\text{in}} - B_{\infty} r^2 / 2$, we obtain $\psi_{\text{in}} = B_{\infty} r_{\text{out}}^2$.

B.3. Solution near the Inner Boundary

Next we show how K_{ϕ} behaves near the inner boundary $r \sim r_{\text{in}}$. We take r_{out} to be infinitely large and approximate ψ_d with

a constant ψ_{in} . As we did for the outer boundary, we assume the solution of the form $K_{\phi}(r') = (c\psi_{\text{in}}/2\pi r'^2) f_{\text{in}}(r')$ where f_{in} approaches unity as $r'/r_{\text{in}} \rightarrow \infty$.

Let us expand f_{out} as

$$f_{\text{in}}(r') = 1 + \sum_{m=1}^{\infty} b_{2m} \left(\frac{r'}{r_{\text{in}}} \right)^{-2m}, \quad (\text{B21})$$

where b_{2m} ($m = 1, 2, \dots$) are constants. We have assumed that f_{in} is an even function of r' because otherwise the resulting $\psi_d(r)$ would involve unwanted logarithmic terms. Substituting Equation (B21) into Equation (B4), performing integration, and using Equation (B12), we obtain

$$\psi_d = \psi_{\text{in}} + \frac{\psi_{\text{in}}}{2} \sum_{n=0}^{\infty} c_n \left(\frac{r_{\text{in}}}{r} \right)^{2n+1} \left[-\frac{1}{2n+1} + \sum_{m=1}^{\infty} \frac{b_{2m}}{2(m-n)-1} \right]. \quad (\text{B22})$$

Since this must be equal to ψ_{in} , b_{2m} ($m = 1, 2, \dots$) must satisfy the relation

$$\sum_{m=1}^{\infty} \frac{b_{2m}}{2(m-n)-1} = \frac{1}{2n+1}, \quad n = 0, 1, \dots \quad (\text{B23})$$

Now let us consider the ansatz

$$f_{\text{in}}(r) = \left[1 - \left(\frac{r'}{r_{\text{in}}} \right)^{-2} \right]^{-\kappa}, \quad (\text{B24})$$

where κ is a constant (cf. Equation (B8)). We require $\kappa < 1$ in order for the radially integrated surface current to be finite. Equation (B24) is equivalent to Equation (B21) with

$$b_{2m} = \frac{(-1)^m}{m!} \frac{\Gamma(1-\kappa)}{\Gamma(1-m-\kappa)}, \quad m = 1, 2, \dots \quad (\text{B25})$$

It can be shown that b_{2m} given by Equation (B25) satisfies

$$\sum_{m=1}^{\infty} \frac{b_{2m}}{2(m-n)-1} = \frac{1}{2n+1} + \frac{\Gamma(-\frac{1}{2}-n)\Gamma(\kappa-1)}{2\Gamma(\frac{1}{2}-n-\kappa)}. \quad (\text{B26})$$

The poles of $\Gamma(-\frac{1}{2}-n-\kappa)$ suggest that Equation (B23) holds for all $n (= 0, 1, 2, \dots)$ when $\kappa = 1/2, 3/2, 5/2, \dots$. Among them, only $\kappa = 1/2$ is the physical solution since the others do not satisfy $\kappa < 1$. Thus, we find that f_{in} is exactly given by Equation (B24) with $\kappa = 1/2$.

C. DISK-INDUCED FLUX IN REGIONS I AND III

Here we derive full analytic expressions for the disk-induced flux ψ_d and corresponding field strength $B_{z,d}$ in regions I and III. From the definition of the flux function (Equation (2)), the disk-induced field strength is given by

$$B_{z,d} = \frac{1}{r} \frac{\partial \psi_d}{\partial r}. \quad (\text{C1})$$

C.1. Region I

As we did in Appendix B, we perform the integration in Equation (41) by expanding the kernel $R(r, r')$ in powers of r/r' . Applying Equations (B1) and (B2) to region I where $r < r_{\text{in}} < r'$, we obtain an equation similar to Equation (B4),

$$\psi_{d,I} = \frac{\pi}{c} \sum_{n=0}^{\infty} c_n r^{2(n+1)} \int_{r_{\text{in}}}^{r_{\text{out}}} \frac{K_{\phi}(r')}{r'^{2n+1}} dr'. \quad (\text{C2})$$

Below we will assume $r_{\text{out}} \rightarrow \infty$ since the contribution of the outer boundary to $\psi_{d,I}$ is small.

Inserting the current density given by Equation (39) into the above equation and neglecting the correction factor f_{out} for the outer boundary, we have

$$\psi_{d,I} = \frac{1}{2} B_{\infty} r_{\text{out}}^2 \sum_{n=0}^{\infty} c_n r^{2(n+1)} \int_{r_{\text{in}}}^{\infty} \frac{f_{\text{in}}(r')}{r'^{2n+3}} dr', \quad (\text{C3})$$

where the correction factor f_{in} for the inner boundary is given by Equation (38). The integral can be reduced, by introducing a variable $x = (r_{\text{in}}/r)^2$, to

$$\int_{r_{\text{in}}}^{\infty} \frac{f_{\text{in}}(r')}{r'^{2n+3}} dr' = \frac{\int_0^1 x^n (1-x)^{-1/2} dx}{2 r_{\text{in}}^{2(n+1)}} = \frac{B(n+1, \frac{1}{2})}{2 r_{\text{in}}^{2(n+1)}}, \quad (\text{C4})$$

where $B(x, y)$ is the Beta function. It can also be shown with *Mathematica* that

$$\sum_{n=0}^{\infty} c_n B(n+1, \frac{1}{2}) \left(\frac{r}{r_{\text{in}}} \right)^{2(n+1)} = 4 - 4 \sqrt{1 - \left(\frac{r}{r_{\text{in}}} \right)^2}. \quad (\text{C5})$$

Using these relations, we finally obtain

$$\psi_{d,I} = B_{\infty} r_{\text{out}}^2 \left[1 - \sqrt{1 - \left(\frac{r}{r_{\text{in}}} \right)^2} \right]. \quad (\text{C6})$$

From Equation (C1), we also obtain the strength of the induced vertical field,

$$B_{z,d,I} = \left(\frac{r_{\text{out}}}{r_{\text{in}}} \right)^2 \frac{B_{\infty}}{\sqrt{1 - (r/r_{\text{in}})^2}}. \quad (\text{C7})$$

Note that $B_{z,I} \gg B_{\infty}$ and hence $B_z \approx B_{z,d,I}$. In the limit of $r \ll r_{\text{in}}$, Equations (C6) and (C7) reduces to Equations (43) and (44) in the main text, respectively.

C.2. Region III

Similarly, we perform the integration in Equation (42) by expanding $R(r', r)$ using Equations (B1) and (B2). Noting that $r' < r_{\text{out}} < r$ for region III, we obtain

$$\psi_{d,I} = \frac{\pi}{c} \sum_{n=0}^{\infty} c_n r^{-(2n+1)} \int_{r_{\text{in}}}^{r_{\text{out}}} r'^{2(n+1)} K_{\phi}(r') dr'. \quad (\text{C8})$$

Below we will assume $r_{\text{in}} \rightarrow 0$ and neglect the contribution of the inner boundary to $\psi_{d,III}$.

Inserting Equation (39) into the above equation and neglecting the inner correction factor f_{in} , we have

$$\psi_{d,III} = \frac{1}{2} B_{\infty} r_{\text{out}}^2 \sum_{n=0}^{\infty} c_n r^{-(2n+1)} \int_0^{r_{\text{out}}} r'^{2n} f_{\text{out}}(r') dr', \quad (\text{C9})$$

where f_{out} is given by Equation (33). By introducing a variable $y = (r/r_{\text{out}})^2$, the integration can be performed as

$$\begin{aligned} & \int_0^{r_{\text{out}}} r'^{2n} f_{\text{out}}(r') dr' \\ &= \frac{r_{\text{out}}^{2n+1}}{2} \int_0^1 \left[y^{n-\frac{1}{2}} - y^n + y^n (1-y^n)^{\gamma} \right] dy \\ &= \frac{r_{\text{out}}^{2n+1}}{2} \left[\frac{1}{1+3n+2n^2} + B(1+n, 1+\gamma) \right], \end{aligned} \quad (\text{C10})$$

where $B(x, y)$ is again the Beta function. It can then be shown with *Mathematica* that

$$\begin{aligned} & \sum_{n=0}^{\infty} c_n \left[\frac{1}{1+3n+2n^2} + B(1+n, 1+\gamma) \right] \left(\frac{r_{\text{out}}}{r} \right)^{2(n+1)} \\ &= \frac{2r}{r_{\text{out}}} \left[F\left(-\frac{1}{2}, -\frac{1}{2}, 1, \frac{r_{\text{out}}^2}{r^2}\right) - F\left(-\frac{1}{2}, \frac{1}{2}, 1+\gamma, \frac{r_{\text{out}}^2}{r^2}\right) \right], \end{aligned} \quad (\text{C11})$$

where $F(a, b, c; z)$ is the hypergeometric function. Using these relations, $\psi_{d,III}$ can be written as

$$\psi_{d,III} = \frac{B_{\infty} r r_{\text{out}}}{2} \left[F\left(-\frac{1}{2}, -\frac{1}{2}, 1, \frac{r_{\text{out}}^2}{r^2}\right) - F\left(-\frac{1}{2}, \frac{1}{2}, 1+\gamma, \frac{r_{\text{out}}^2}{r^2}\right) \right], \quad (\text{C12})$$

and from Equation (C1), we also obtain the induced vertical field

$$B_{z,d,III} = \frac{r_{\text{out}}}{r} \left[\frac{2}{\pi} E\left(\frac{r_{\text{out}}^2}{r^2}\right) - F\left(\frac{1}{2}, \frac{1}{2}, 1+\gamma, \frac{r_{\text{out}}^2}{r^2}\right) \right]. \quad (\text{C13})$$

The asymptotic form of $\psi_{d,II}$ at $r \gg r_{\text{out}}$ can be easily obtained by dropping the $n \geq 1$ terms in Equation (C9), namely,

$$\begin{aligned} \psi_{d,III} &\approx \frac{B_{\infty} r_{\text{out}}^2}{2r} \int_0^{r_{\text{out}}} f_{\text{out}}(r') dr' \\ &\approx \frac{B_{\infty} r_{\text{out}}^3}{4r} [1 + B(1, 1+\gamma)] \approx 0.425 \frac{B_{\infty} r_{\text{out}}^3}{r}, \end{aligned} \quad (\text{C14})$$

where we have used that Equation (C10), $c_0 = 1$, and $B(1, 1+\gamma) \approx 0.7$ for the best-fit parameter $\gamma = 0.43$ (see Appendix B.2). The corresponding B_z is

$$B_{z,d,III} \approx -0.425 \left(\frac{B_{\infty} r_{\text{out}}}{r} \right)^3. \quad (\text{C15})$$

REFERENCES

- Andrews, S. M., Wilner, D. J., Hughes, A. M., Qi, C., & Dullemond, C. P. 2009, *ApJ*, 700, 1502
- Agapitou, V., & Papaloizou, J. C. B. 1996, *Astrophys. Lett. Commun.*, 34, 363
- Allen, A., Shu, F. H., & Li, Z.-Y. 2003, *ApJ*, 599, 351
- Bai, X.-N. 2011, *ApJ*, 739, 50
- Bai, X.-N. 2013, *ApJ*, 772, 96
- Bai, X.-N., & Stone, J. M. 2013a, *ApJ*, 767, 30
- Bai, X.-N., & Stone, J. M. 2013b, *ApJ*, 769, 76
- Balbus, S. A., & Hawley, J. F. 1991, *ApJ*, 376, 214
- Balbus, S. A., & Hawley, J. F. 1998, *RvMP*, 70, 1
- Beckwith, K., Hawley, J. F., & Krolak, J. H. 2009, *ApJ*, 707, 428
- Bisnovatyi-Kogan, G. S., & Lovelace, R. V. E. 2007, *ApJL*, 667, L167
- Bisnovatyi-Kogan G. S., & Lovelace R. V. E., 2012, *ApJ*, 750, 109
- Bisnovatyi-Kogan G. S., & Runzmaikin, A. A., 1974, *Ap&SS*, 28, 45
- Blandford, R. D., & Payne, D. G. 1982, *MNRAS*, 199, 883
- Braithwaite, J. 2012, *MNRAS*, 422, 619
- Brandenburg, A., Nordlund, A., Stein, R. F., & Torkelsson, U. 1995, *ApJ*, 446, 741
- Calvet, N., Muzerolle, J., Briceño, C., et al. 2004, *AJ*, 128, 1294
- Cao, X., & Spruit, H. C. 2002, *A&A*, 385, 289
- Crutcher, R. M., Hakobian, N., & Troland, T. H. 2009, *ApJ*, 692, 844
- Dapp, W. B., Basu, S., & Kunz, M. W. 2012, *A&A*, 541, A35
- Davis, S. W., Stone, J. M., & Pessah, M. E. 2010, *ApJ*, 713, 52
- Dzyurkevich, N., Turner, N. J., Henning, T., & Kley, W. 2013, *ApJ*, 765, 114
- Flock, M., Dzyurkevich, N., Klahr, H., Turner, N., & Henning, T. 2012a, *ApJ*, 744, 144
- Flock, M., Henning, T., & Klahr, H. 2012b, *ApJ*, 761, 95
- Fromang, S., & Stone, J. M. 2009, *A&A*, 507, 19
- Galli, D., Lizano, S., Shu, F. H., & Allen, A. 2006, *ApJ*, 647, 374
- Galli, D., & Shu, F. H. 1993, *ApJ*, 417, 220
- Gressel, O. 2010, *MNRAS*, 405, 41
- Gressel, O., Nelson, R. P., & Turner, N. J. 2012, *MNRAS*, 422, 1240
- Guan, X., & Gammie, C. F. 2009, *ApJ*, 697, 1901
- Guilet, J., & Ogilvie, G. I. 2012, *MNRAS*, 424, 2097
- Guilet, J., & Ogilvie, G. I. 2013, *MNRAS*, 430, 822
- Hartmann, L., Calvet, N., Gullbring, E., & D'Alessio, P. 1998, *ApJ*, 495, 385

- Hawley, J. F., Gammie, C. F., & Balbus, S. A. 1995, *ApJ*, 440, 742
- Hayashi, C. 1981, *Prog. Theor. Phys. Suppl.*, 70, 35
- Jackson, J. D. 1998, *Classical Electrodynamics* (3rd ed.; New York: Wiley)
- Johns-Krull, C. M. 2007, *ApJ*, 664, 975
- Johnson, K. L. 1987, *Contact Mechanics* (Cambridge: Cambridge Univ. Press)
- Kitamura, Y., Momose, M., Yokogawa, S., Kawabe, R., Tamura, M., & Ida, S. 2002, *ApJ*, 581, 357
- Kunz, M. W., & Lesur, G. 2013, *MNRAS*, 434, 2295
- Landau, L. D., & Lifshitz, E. M. 1986, *Theory of Elasticity* (3rd ed; Oxford: Butterworth-Heinemann)
- Lesur, G., & Longaretti, P.-Y. 2009, *A&A*, 504, 309
- Li, Z.-Y., & Shu, F. H. 1997, *ApJ*, 475, 237
- Lovelace, R. V. E. 1976, *Natur*, 262, 649
- Lovelace, R. V. E., Rothstein, D. M., & Bisnovatyi-Kogan, G. S. 2009, *ApJ*, 701, 885
- Lubow, S. H., Papaloizou, J. C. B., & Pringle, J. E. 1994a, *MNRAS*, 267, 235 (LPP94a)
- Lubow, S. H., Papaloizou, J. C. B., & Pringle, J. E. 1994b, *MNRAS*, 268, 1010
- Machida, M. N., Inutsuka, S., & Matsumoto, T. 2007, *ApJ*, 670, 1198
- Moll, R. 2012, *A&A*, 548, A76
- Murray, C. D., & Dermott, S. F. 1999, *Solar System Dynamics* (Cambridge: Cambridge Univ. Press)
- Nakano, T. 1984, *Fundam. Cosmic Phys.*, 9, 139
- Nakano, T., Nishi, R., & Umebayashi, T. 2002, *ApJ*, 573, 199
- Ogilvie, G. I. 1997, *MNRAS*, 288, 63
- Ogilvie, G. I., & Livio, M. 2001, *ApJ*, 553, 158
- Okuzumi, S., & Hirose, S. 2011, *ApJ*, 742, 65
- Pessah, M. E., Chan, C.-K., & Psaltis, D. 2007, *ApJ*, 668, L51
- Rothstein, D. M., & Lovelace, R. V. E. 2008, *ApJ*, 677, 1221
- Sano, T., Inutsuka, S., Turner, N. J., & Stone, J. M. 2004, *ApJ*, 605, 321
- Shu, F. H., Galli, D., Lizano, S. & Cai, M. 2006, *ApJ*, 647, 382
- Sicilia-Aguilar, A., Hartmann, L. W., Hernández, J., Briceño, C., & Calvet, N. 2005, *AJ*, 130, 188
- Simon, J. B., Bai, X.-N., Stone, J. M., Armitage, P. J., & Beckwith, K. 2013a, *ApJ*, 764, 66
- Simon, J. B., Bai, X.-N., Stone, J. M., Armitage, P. J., & Beckwith, K. 2013b, *ApJ*, in press
- Simon, J. B., Hawley, J. F., & Beckwith, K. 2011, *ApJ*, 730, 94
- Spruit, H. C. 1996, in *Evolutionary Processes in Binary Stars*, ed. R. A. M. J. Wijers, M. B. Davies, & C. A. Tout (NATO ASI Series C, 477; Dordrecht: Kluwer), 249
- Spruit H. C., & Uzdensky D. A. 2005, *ApJ*, 629, 960
- Suzuki, T. K., & Inutsuka, S. 2013, *ApJ*, submitted (arXiv:1309.6916)
- Suzuki, T. K., Muto, T., & Inutsuka, S. 2010, *ApJ*, 718, 1289
- Takeuchi, T., & Lin, D. N. C. 2002, *ApJ*, 81, 1344
- Takeuchi, T., & Okuzumi, S. 2013, *ApJ*, submitted (Paper II)
- Troland, T. H., & Crutcher, R. M. 2008, *ApJ*, 680, 457
- van Ballegoijen, A. A. 1989, in *Astrophysics and Space Science Library*, Vol. 156, *Accretion Disks and Magnetic Fields in Astrophysics*, ed. G. Belvedere (Dordrecht: Kluwer), 99
- Wardle, M. 2007, *Ap&SS*, 311, 35
- Wardle, M., & Salmeron, R. 2012, *MNRAS*, 422, 2737